NON-MIGRATING TIDES IN THE MARTIAN THERMOSPHERE

Aishwarya Sukesh Kumar

Thesis submitted to the Faculty of the
Virginia Polytechnic Institute and State University
in partial fulfillment of requirements for the degree of

Master of Science
in
Electrical Engineering

Scott M. Bailey, Chair
Scott L. England
Elena S. Lind

August 2, 2018
Blacksburg, Virginia

Keywords: Non-migrating tides, density, $CO_2^+ UV\ doublet$, MAVEN, IUVS

NON-MIGRATING TIDES IN THE MARTIAN THERMOSPHERE

Aishwarya Sukesh Kumar

ABSTRACT

Previous studies have identified longitudinal structures associated with non-migrating tides in observations of the upper neutral atmosphere of Mars. MAVEN's Imaging Ultraviolet Spectrometer (IUVS) observations of the upper atmosphere reveal variations in density with longitude at altitudes of 130 – 200 km, and can be used to identify non-migrating tides. These observations cover higher latitudes and allow for studying the local time variations of tides. The analysis presented here shows that the longitudinal structure attributed to non-migrating tides is dominated by wavenumber 2 and wavenumber 3 harmonics during the periods studied. Comparison with the Neutral Ion and Gas Mass spectrometer (NGIMS) shows a good agreement in wave amplitudes observed for the first two cases studied. The temperatures and O/CO_2 ratios from the IUVS L2 data files revealed an anti-correlation with the densities which confirms the theoretical interpretation from the linear wave theory.

NON-MIGRATING TIDES IN THE MARTIAN THERMOSPHERE

Aishwarya Sukesh Kumar

GENERAL AUDIENCE ABSTRACT

There are waves internal to all fluids in our surroundings and daily lives, such as sound waves. Waves in the atmosphere are also fluid in nature. In planetary atmospheres, the scale sizes of some of these waves become comparable to the size of the planet itself. The waves interact with the structure of the surface of Mars to form a certain type of wave called "Non-migrating tides". These waves have been observed in multiple previous studies in the upper atmosphere of Mars (~130 km and above). These waves cause the atomic and molecular content of the upper atmosphere to be displaced in a particular manner to form a unique structure. The structures formed are observed on a scale that covers the entire planet. It is by studying these structures in the upper atmosphere that it is possible to characterize the waves that control them and thereby understand their nature and impact. Understanding how these waves vary helps spacecraft to gain better control over mechanisms required to swing them into the desired orbit (location).

This study uses the observations from an instrument aboard the MAVEN mission and compares it to the observations from another instrument aboard the same mission. The results of this study demonstrate that these "Non-migrating" tides play a vital role in controlling the behavior of the upper atmosphere.

Acknowledgements

I would like to thank Dr. Scott England for his guidance and patience throughout this project. I would also like to give thanks to Dr. Scott Bailey for helping me choose a project that I would love to work on and Dr. Elena Lind for her invaluable advice for writing my thesis. A special thanks to Dr. Guiping Liu without whose help this project would not have been possible.

Dedication

To my loving family in India and in the Unites States, my friends who are no less than family in Blacksburg with whom I cherished chai time and lovely conversations.

Table of Contents

List of Figures

List of Tables

1 Introduction

Mars has been of great interest with decades of missions sent to explore its habitability. It has been long studied with the first successful flyby by the Mariner 4 spacecraft dating back to 1965. There has been abundant geological and geochemical evidence from observations made in the past two decades that indicate the existence of water on the surface or below the surface of Mars in the past and possibly in the present (Jakosky et al., 2015). Small and strong crustal magnetic fields tied to the heavily cratered terrain have been detected, indicating that Mars may have had an internal dynamo in the past which may now be extinct (Acuña, 1999).These new findings combined with the objective of deploying a manned mission to Mars in the coming decade has propelled further interest in finding answers to questions such as "How did Mars loose its water?", "Where did its magnetic field go?" and so on. To tackle these questions, it is important to understand the evolution of the Martian atmosphere.

Chapter 1 will introduce the motivation and goal for this thesis. Section 1.1 introduces the common characteristics that Mars shares with the Earth, 1.2 discusses the upper atmosphere of Mars and previous observations of the upper atmosphere, 1.3 introduces atmospheric tides, their role in controlling the dynamics of the upper atmosphere and previous observations of tides in Mars' upper atmosphere, 1.4 discusses the MAVEN mission and its goals, 1.5 describes the Imaging Ultraviolet Spectrograph aboard the MAVEN spacecraft from which data has been acquired for analysis in this thesis, 1.6 discusses observations of atmospheric tides using MAVEN data.

1.1 Mars and its atmosphere

'Mars', also known as the red planet for its rusty orange-red color which is attributed to iron oxides, is the fourth planet in our solar system. Table 1 summarizes a list of parameters that highlight the similarities and differences between Mars and the Earth. With a size half as much as that of the Earth, Mars shares some striking similarities with the Earth. Its rotation rate is similar to the Earth's and experiences seasons due to its axial tilt. It is placed in a more eccentric orbit around the Sun than Earth, with perihelion at 1.38 AU and aphelion at 1.66 AU which results in more drastic changes in its seasons. It takes nearly twice the number of days taken by the Earth to go around the Sun and surface gravity on Mars is much weaker than it is on Earth.

Parameters	Mars	Earth
Length of day (hours)	24.6597	24
Surface gravity (m/s^2)	3.71	9.8
Orbit period (days)	686.98	365.256
Axial tilt (degrees)	25.19	23.44
Orbital eccentricity	0.094	0.017
Solar irradiance (W/m^2)	586.2	1361
Surface pressure (bar)	0.01	1
Global magnetic field	No	Yes
Scale height (km)	11.1	8.5

Table 1: Comparison of a few orbital parameters and atmospheric characteristics of Mars and Earth. Source https://nssdc.gsfc.nasa.gov/planetary/factsheet/marsfact.html

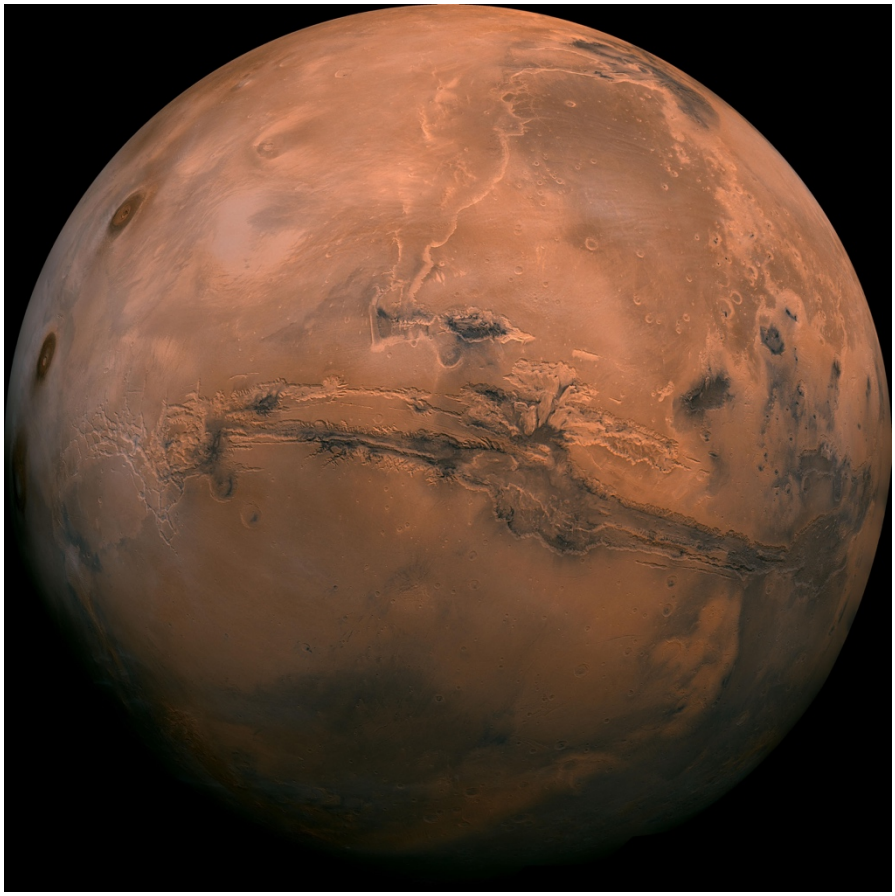

Figure 1: An enhanced picture of the Valles Marineris created by 102 Viking orbiter images of Mars. It is a huge canyon that runs 4000 km long and upto 7 kms deep. The features of the surface can be seen carefully.

Figure 1 shows a picture of the largest canyon network on Mars, the Valles Marineris. This canyon reaches a depth of upto 7 km which is shy of a few kilometers from the scale height of Mars which is 11.1 km in the lower atmosphere. The Grand Canyon in our home planet on the otherhand runs about 1.6 km deep and is about $1/5^{th}$ the scale height of the Earth's atmosphere. The primary constituent making up most of Mars' atmosphere is carbon dioxide, which is followed by nitrogen, argon, oxygen and carbon monoxide (Haberle et al., 2017). As seen in Table 1, the surface pressure on Mars is very low, about 1% of the Earth's. The temperatures in the Martian atmosphere are strongly controlled by the suspended dust particles, which scatter sunlight.

The vertical structure of the atmosphere can be described by change in temperature as a function of altitude. The atmosphere of the Earth is divided into various regions based on this temperature gradient into the troposphere, stratosphere, mesosphere and thermosphere. The atmosphere of Mars is more broadly classified into the lower, middle and upper atmosphere as shown in Figure 2a. This structure when compared to that of Earth's shows that Mars does not have a stratosphere due to lack of an ozone layer. The figure also highlights the role of dust in changing the temperature and temperature structure of the Martian atmosphere.

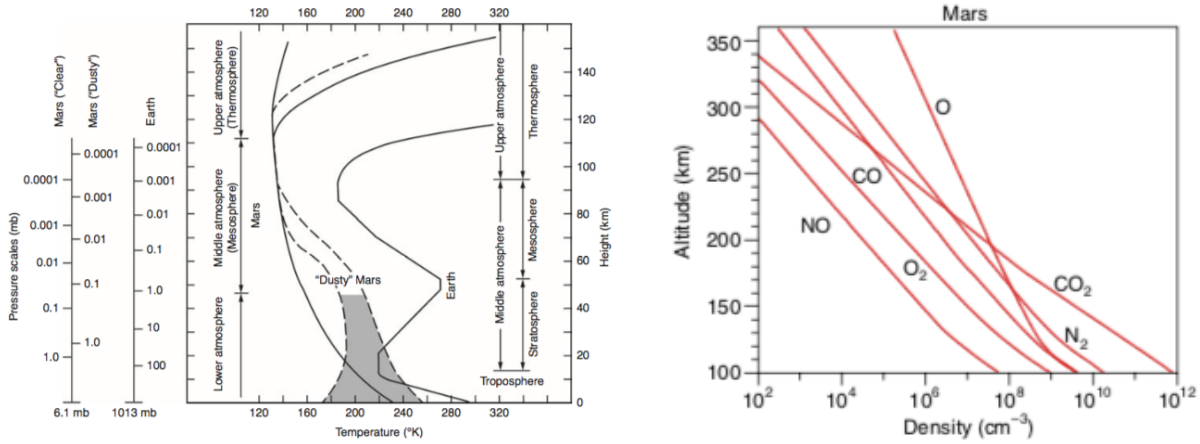

Figure 2: a) Figure from Haberle et al. 2017 shows the vertical structure of Earth and Mars. The vertical structure on Mars is seen to vary during the onset of duststorms. b) Figure from Mendillo et al., 2018 shows the compositon of neutral species in Mars.

1.2 Upper atmosphere

The upper atmosphere of a planet comprises the Thermosphere, Ionosphere and the Exosphere. Mars' upper atmosphere is a channel that connects the lower atmosphere near the surface of the planet to the nearby interplanetary environment. The upper atmosphere of Mars has not been studied extensively owing to the restricted number of observations that are scattered through select locations and at different periods during the solar cycle. However, the Martian upper atmosphere plays an important role in regulating the escape of atmospheric species, which in turn is essential to understand the evolution of the entire atmosphere. The composition and structure of the upper atmosphere and the mechanisms that effect them are not well known. Any atmospheric model is incomplete without an understanding of the upper atmosphere.

Another crucial reason to study the upper atmosphere is because spacecraft's generally perform aerobraking maneuvers in this region, contributing to huge savings by reduction in fuel costs. The spacecraft uses atmospheric drag to decelerate the spacecraft's velocity to achieve orbit insertion in its desired orbit. Mars Global Surveyor (MGS), Mars Reconnaissance Orbiter (MRO) and Mars Odyssey are some of the missions that used the aerobraking process to gradually insert itself into their respective desired orbits (Haberle et al., 2017). Performing such maneuvers requires comprehensive knowledge of the density structure and variability in order to minimize risks.

Two major driving sources of the dynamics of Earth's upper atmosphere are a) interaction with its strong intrinsic magnetic field and B) the solar UV and EUV processes. In Mars, the primary driving force is the solar UV and EUV processes alone since it lacks a global magnetic field (Bougher et al., 1999). Figure 2a shows that the Martian thermosphere begins at ~120 km. The homopause which is located ~125 km distinguishes the thermosphere from the region below where molecular constituents are well mixed (Bougher et al., 2015). The most abundant species in the thermosphere of Mars in CO_2 and its dissociation products CO and O and can be seen in Figure 2b.

"The thermosphere is an intermediate atmospheric region strongly coupled to the lower-middle atmosphere by gravity waves, planetary waves, thermal tides, dust storms etc. and also coupled from above with the energy inputs from the Sun by Solar X-ray, EUV and UV fluxes and solar wind particles." - (Haberle et al., 2017). Therefore, understanding the chemical and physical processes taking place in this region is key to understanding the flow of energy and material into and out of the planet.

The thermospheric characteristics of Mars are highly variable on various temporal scales due to change in its heliocentric distance which can vary between ~1.38 and 1.67 A.U., its axial tilt and change in the solar input, both in the form of solar radiation and solar wind. The density structure of the thermosphere has been measured by accelerometers on multiple spacecraft's such as the MGS, Odyssey and MRO. Mars Odyssey found that the thermospheric temperatures increase with latitude near the northern winter pole (Keating et al., 2003).

Observations from the MGS aerobraking phases revealed longitudinal variations in densities in the upper atmosphere (Keating et al., 1998). The density structures observed during the MGS aerobraking campaigns are attributed to atmospheric tides. It is these tides that will be the topic of interest hereafter with an effort to understand how they control densities of neutrals in the thermosphere.

1.3 Atmospheric thermal tides

Solar atmospheric tides or atmospheric thermal tides refer to global scale oscillations or perturbations produced due to the thermal effects of the sun on a planetary atmosphere. The primary driving mechanism of atmospheric tides is the diurnal (day/night variation) absorption of solar heat by a rotating atmosphere. The period of these tides are harmonics of a sol ('sol' for Mars is equivalent to a solar 'day' on Earth). Atmospheric tides have a crucial role in controlling the dynamics of the atmosphere (Bougher et al., 2001; Forbes and Hagan, 2000; Keating et al., 2003; Withers et al., 2003). These waves can be inferred by the horizontal and vertical oscillations in quantities such as the density and temperature. The tidal oscillations can be mathematically represented by the following expression:

$$A(z,\theta).\cos\left(n\Omega t + s\lambda - \phi_n(z,\theta)\right) \dots\dots\dots\dots [1]$$

where A is the amplitude, $\Omega = 2\pi\ sol^{-1}$ is the planetary rotation rate and varies from 0 to 2π over a day (or sol in this case), t is the universal time in sols, λ is the longitude with east positive, ϕ_n is the phase of the wave, s is the zonal wavenumber and its absolute value is the number of cycles per $360°$ longitude, n is the temporal harmonic and provides the number of waves per sol (Forbes and Hagan, 2000). Components with $n = 1$ for the diurnal tide has a period of one day, $n = 2$ for the semi-diurnal tide which has a period of half a day and so on. Components with $s > 0$ propagate westwards, $s < 0$ propagate eastward. As can be seen in the above expression, the amplitude and the phase are both functions of altitude and the latitude.

Equation [1] describes a tide in a fixed universal time (UT) frame, where a tide with $|s| = 1$ consists of one cycle per $360°$ longitude known as wave number 1, a tide with $|s| = 2$ consists of two cycles per $360°$ longitude known as wave number 2 and so on.

It is useful to note that the mean period of a solar day on Mars is 24 hours 39 minutes 35.244 seconds which is nearly 3% longer that a solar day on Earth ("Mars24 Sunclock — Time on Mars," n.d.). A 'day' on Earth is analogous to 'sol' on Mars. The word 'diurnal' refers to a 'a sol'. An 'hour' on Mars corresponds to a rotation of 15° about its own axis.

Following (Forbes and Hagan, 2000), rewriting the above expression in terms of local time, where $t = t_{LT} - \frac{\lambda}{2\pi}$ we get,

$$A(z,\theta).\cos\left(n\Omega\left(t_{LT} - \frac{\lambda}{2\pi}\right) + s\lambda - \phi_n(z,\theta)\right) \dots\dots\dots\dots [2]$$

$$A(z,\theta).\cos\left(n\Omega t_{LT} - n\Omega\frac{\lambda}{2\pi} + s\lambda - \phi_n(z,\theta)\right)$$

$$A(z,\theta).\cos\left(n\Omega t_{LT} - n\lambda + s\lambda - \phi_n(z,\theta)\right)$$

$$A(z,\theta).\cos\left(n\Omega t_{LT} + \lambda(s-n) - \phi_n(z,\theta)\right) \dots\dots\dots\dots\dots [3]$$

From equation [3], for a fixed local-time reference frame, or in other words for an observer on the ground, the $s = n$ components of the tide will move with the same speed as the Sun in the sky. The $s = n$ components imply that the number of cycles per 360° longitude is the same as the number of cycles observed in a single day. By substituting $s = n$ in equation [3] we also see that the amplitude of these waves are independent of longitude in this reference frame. These are called migrating tides. For an observer on the ground, the zonal phase speed of migrating tides is equal to the speed of the Sun. In a fixed LT frame, a tide with $|\ s = n\ |$ = 1 will consist of one cycle per 360° longitude known as wave-1. The data used in this study will provide us with this wavenumber denoted by $|\ s = n\ |$, but we would like to know the individual values of n and s as well.

Non-migrating tides are those components for which $s \neq n$. The interaction of solar forcing with the topography of Mars, in other words the zonal asymmetries of the planet produce non-migrating tides (Zurek, 1976). These tides can vary with longitude in a fixed local time frame unlike migrating tides.

If the topographic component is represented by:

$$\cos(m\lambda - \phi_m) \dots\dots\dots\dots [4] \qquad \text{(Forbes and Hagan, 2000)}$$

then its interaction with the (s = n) migrating tides represented by equation [1] will yield:

$$\cos(n\Omega t + n\lambda - \phi_n) * \cos(m\lambda - \phi_m) \dots\dots\dots\dots\dots\dots\dots [5]$$

Using trigonometric identities, we can rewrite equation [5] as:

$$\cos(n\Omega t + n\lambda - \phi_n - m\lambda + \phi_m) + \cos(n\Omega t + n\lambda - \phi_n + m\lambda - \phi_m)$$

$$\cos(n\Omega t + (n-m)\lambda - (\phi_n - \phi_m) + \cos\left((n\Omega t + (n+m)\lambda - (\phi_n + \phi_m)\right) \dots\dots\dots [6]$$

The above equation [6] can be encapsulated as sum and difference terms:

$$\cos(n\Omega t + (n \pm m)\lambda - (\phi_n \pm \phi_m) \ldots\ldots\ldots\ldots [7]$$

The equation [7] describes a tide that has a period given by 'n' and a zonal wavenumber of '$n \pm m$'. Therefore, the $n = 1$, dirunal component of solar migrating radiation interacts with $m = 2$ component of topography to produce diurnal tides that propagate westward with $s = 3$ and eastward with $s = -1$. This can also be seen in Figure 3 which depicts this interaction to produce non-migrating tides. The table below summarizes the wavenumbers generated by the interaction of the migrating solar radiation with the topographic component (topographic wavenumber).

Migrating solar radiation component (n)	Topographic wavenumber component (m)	Wavenumbers (s = n±m)	
		n + m	n - m
1	1	2	0
1	2	3	-1
2	1	3	1
2	2	4	0

Table 2: Wavenumber s = n±m produced by the interaction of migrating solar radiation frequency component with the topographic component adapted from (Forbes et al., 2002).

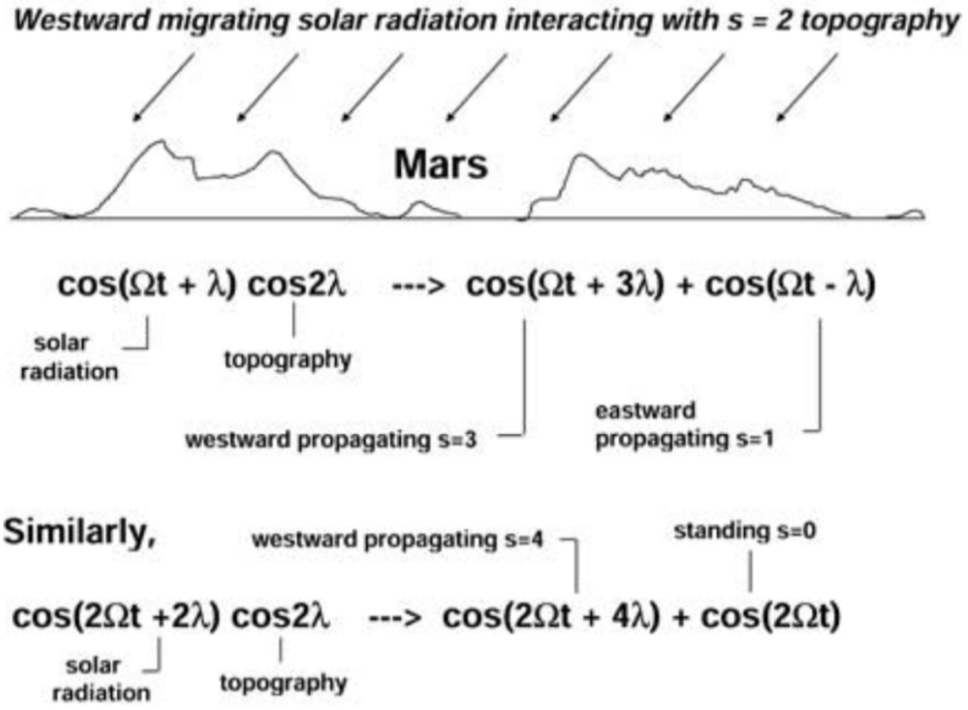

Figure 3: Depicts the interaction of the migrating tide (or the tide excited due to solar radiation) with the topography of Mars to produce non-migrating tides consisting various wavenumbers. Picture from Forbes et al., 2002.

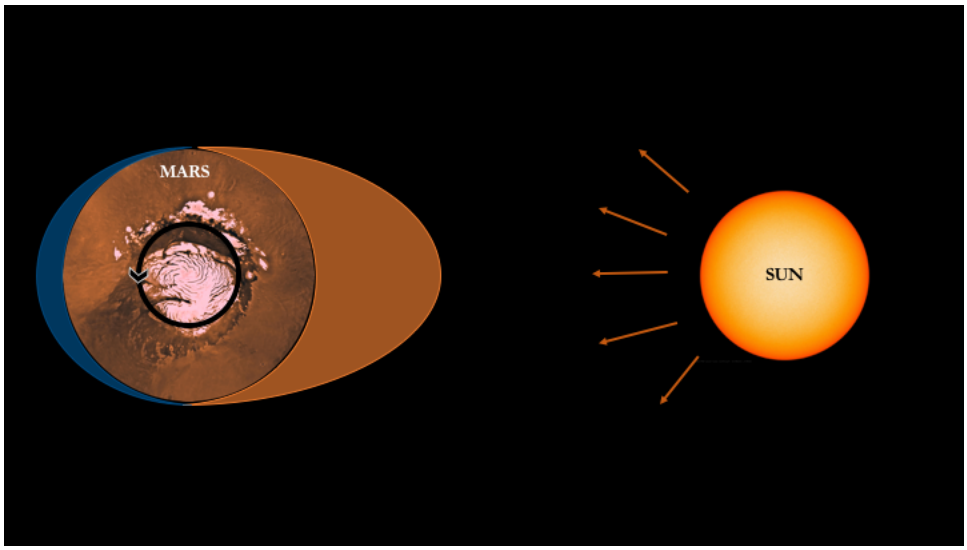

Figure 4: Adapted from https://mars.nasa.gov/resources/4872/thermal-tides-at-mars/. Figure shows tides produced due to the heating of the rotating atmosphere of Mars in the Mars-Sun frame.

Regardless of their production mechanism, this study will be focused on non-migrating tides, specifically the tides with wavenumber 2 and wavenumber 3, in a fixed LT frame. By referring to equation [3], there are multiple combinations of n and s that can can produce a non-migrating tide with wavenumbers 2 and 3. For instance, a tide with wavenumber $|s - n| = 2$ where $n = 1$ and $s = -1$ has 2 cycles per 360° longitude in a fixed local time reference frame. For the same wavenumber 2, the values of n and s can also be $n = 1$ and $s = +3$; $n = 0$ and $s = 2$; $n = 2$ and $s = 0$ or $n = 2$ and $s = +4$. Here we ignore tides with $n = 3$ and beyond, since they are small but present on Mars. The observational data helps in identifying $|s - n|$, but for a particular observed wavenumber, s and n can take on multiple values from which it can be only one of the combinations. $s > 0$ and $s < 0$ corresponds to westward moving and eastward moving tide respectively.

In order to find the values of s and n, samples of multiple local times over a certain range will be required. In the cases analyzed here the chosen time periods and datasets allow to establish the value of $'n'$ and the sign of $'s'$

Previous studies have been shown that the interaction of solar heating with the topography and atmosphere of Mars gives rise to atmospheric tides which can produce significant perturbations in the densities of neutral species in its upper atmosphere (England et al., 2016; Forbes and Hagan, 2000; Withers et al., 2003).

As mentioned in the previous section, strong longitudinal variations in densities were reported using the accelerometer on the MGS spacecraft (Keating et al., 1998). These variations were attributed to stationary planetary waves consisting a combination of wave numbers 1 and 2. An alternate explanation attributing these longitudinal density variations to non-migrating tides was given using the same data set (Forbes and Hagan, 2000). The motivation for this was based on previously studied modelling results indicating that stationary planetary waves maximize well below the thermospheric altitudes which were being sampled by MGS and that the topography of Mars should have an impact on the waves. Modelling results showed that the density structures

observed had a significant contribution from the diurnal eastward tide (DE1) thereby indicating the role of topographic modulation of tides. It is important to note that although non-migrating tides were interpreted in this study, the results are derived from a model and not from observational data.

Wave number 3 features associated with non-migrating tides were observed in the electron density peak measurements as well as in the accelerometer measurements from the MGS spacecraft (Bougher et al., 2001). Wave number 2 and 3 were found to dominate in the large scale longitudinal variation in densities observed using the MGS accelerometer measurements between altitudes of 130 – 160 km (Withers et al., 2003). Zonal variations in pressure and temperature associated with non-migrating tides were observed using the Mars Express SPICAM UV spectrometer in the middle atmospheric region between 70 and 120 km (Withers et al., 2011). Here also, wave numbers 2 and 3 were found to be dominant.

The longitudinal structures observed are wide spread, have a large amplitude and in most cases are periodic in nature, making it an important phenomenon that must be understood and incorporated into any atmospheric model attempting to describe the atmosphere of Mars. It is useful to note that the solar input received by the planet consist of no zonal inhomogeneties and therefore the zonal structures observed in previous studies have to have originated from the non-uniform topography of Mars (Withers et al., 2003). The zonal structure will be affected by the lower atmosphere as it propagates through it. The observed longitudinal structures will therefore reveal information about the forcing mechanism as well as the characteristics of the lower atmosphere (Zurek, 1976).

A lack of observational data made it difficult to have a complete understanding of the nature of tides and various other atmospheric phenomena. The MAVEN mission was designed in response to the previous studies and evidence of the key role that upper atmospheric dynamics play in the regulation of atmospheric evolution.

1.4 MAVEN

Following the description of (Jakosky et al., 2015), launched in September of 2013, the MAVEN mission arrived at Mars in November 2013 with the goal of unravelling the climate history of Mars. The key emphasis of MAVEN is to study the upper atmosphere, its interactions with the solar wind and the sun and to thereby understand underlying phenomenon leading to loss of atmospheric gas to space. Previous missions to Mars have well established that there has been loss of atmospheric gas to space and that Mars has undergone climate change. The evidence can be categorized into two sections, namely 1) geological and geochemical evidence and 2) loss to space. In the geological front, currently there is almost no water present on the surface of Mars due to the low atmospheric pressure and temperatures, although there is abundant evidence of erosion due to water. The presence of valley networks indicate that Mars had a thicker atmosphere with higher surface temperatures.

As for loss of atmospheric gas to space, multiple observations suggest that it has been happening throughout the planet's history and continues to occur till date. The evolution of the Martian atmosphere has been extensively affected by the escape of lighter gas. The deuterium to hydrogen ratio (D/H) is one such method of inferring loss of atmospheric gas. Deuterium is an isotope of

hydrogen consisting of a neutron in its nucleus making it twice as heavy as hydrogen. The lighter isotope is therefore able to escape easily, having larger scale heights the ratio of light to heavy species increases with increasing altitude. A number of mechanisms have been proposed that lead to escape of crucial atmospheric species. This is done by extrapolating the known dominant escape processes on Earth which includes Jeans escape, Photochemical loss, Ion loss, Pickup Ions and Atmospheric sputtering, Ion Bulk escape and Ion outflow.

To summarize, the goals of the MAVEN mission is to measure the composition and structure of the upper atmosphere of Mars and identify the physical processes that influence and control them, attempt the validation of the previously made observations and theoretical predictions, quantify the rate of loss of gas from the upper atmosphere and the underlying mechanisms controlling them, and lastly attempt to extrapolate back in time to determine the total loss of atmospheric gas to space and relate this to the geological evidence.

In order to meet these goals, the MAVEN spacecraft has nine instruments on board which are grouped into three science packages: Particles and Fields Package, Remote Sensing Package and the Mass Spectrometry Unit. The spacecraft also includes an Articulated Payload Platform (APP) which allows three instruments to point at any direction independent of the direction of the spacecraft. The three instruments mounted on the APP are the Imaging Ultraviolet Spectrograph (IUVS), the Neutral Gas and Ion Mass Spectrometer (NGIMS) and the Supra-Thermal and Thermal Ion Composition (STATIC). The observations from the IUVS instrument are used in this study.

The orbit of MAVEN around Mars is elliptical with a period of 4.5 hours, orbital inclination of 75º, periapsis altitude at ~150 km and apoapsis altitude at 6220 km . The orbital parameters are chosen such that all local solar times and all latitudes between +75º to -75º can be covered. Also important criteria for the chosen geometry are the ability measure solar wind and the atmosphere.

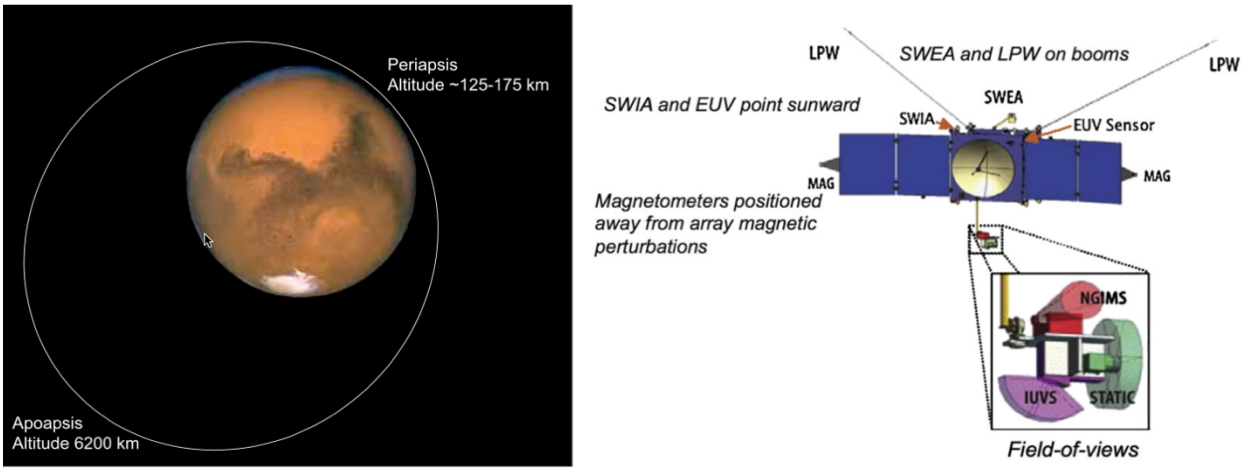

Figure 5: Figures from Jakosky et al., 2015 a) Shows the orbit of MAVEN b) Shows the instruments placed on the spacecraft body. Also shows the instruments placed on the Articulated Payload platform (APP) and their field of views.

1.5 IUVS

As described in (McClintock et al., 2015), the IUVS measures the UV emissions of atmospheric constituents from a distance to derive atmospheric properties. IUVS makes its measurements in an altitude range from the surface to 4500 km. The main goal of the IUVS is to use the observed UV emissions to characterize the structure and composition of the upper atmosphere. The measurements made by IUVS contributes to the MAVEN science goals as it enables the validation of observations made by *in situ* instruments, provides a global context for measurements taken by *in situ* instruments and lastly makes measurements of atmospheric properties that cannot be made by the other instruments.

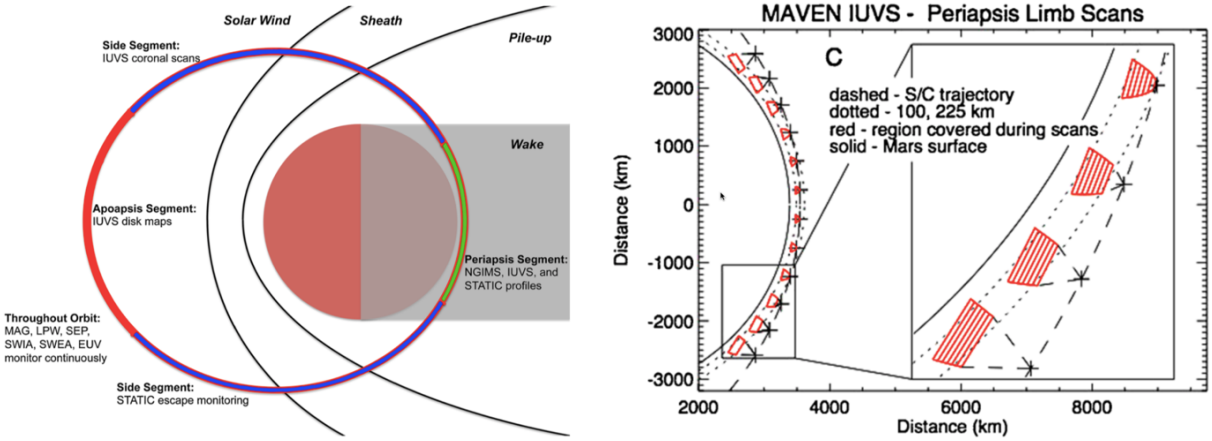

Figure 6: a) Shows the different observational modes of the IUVS. Figure from Jakosky et al., 2015 b) Shows the periapse limb scans in the plane of the spacecraft orbit. The scan mirror scans the limb of Mars, making 12 such scans during the 23-minute portion of the orbit. The IUVS makes 21 measurements during each scan. Figure from McClintock et al., 2015

The observation modes of IUVS can be divided into four categories based on its position in an orbit: Periapse observations, apopase observations, stellar occultations and coronal scans. This is shown in the Figure 6a. As mentioned in section 4.1, IUVS is mounted on the APP which allows it to take measurements independent of the sun-pointing spacecraft.

IUVS is part of the MAVEN remote sensing package. It uses a long, narrow slit (11° x 0.06°) to image the atmosphere onto a plane grating spectrograph. It utilizes a scan mirror that can select between a limb field of regard (24° x 11°) and a nadir field of regard (60° x 11°) and is also used to map and scan the planet. The IUVS consists of an MUV and an FUV detector with spectral resolutions of 1.2 nm and 0.6 nm respectively. The wavelength range for the MUV is 180 – 340 nm and for the FUV is 110 – 190 nm. During the 23-minute periapsis portion of the orbit IUVS scans the limb of the orbit. These observations are made when the spacecraft altitude is below ~500 km. The field of view of the instrument is pointed towards the limb such that it is nearly parallel to the surface of the planet as shown in Figure 7. These are the observations that will be used in the study rather than those taken at any other portion of the orbit.

Sampling in altitude is achieved by moving the field of view vertically by the scan mirror. During a single scan 21 measurements are made at all the altitude steps. IUVS makes 12 such scans during

the periapsis portion of the orbit. Motion within a single scan is negligible, but motion between two consecutive scans is significant. Figure 6b shows the geometry of the periapsis limb scans in the plane of the spacecraft orbit.

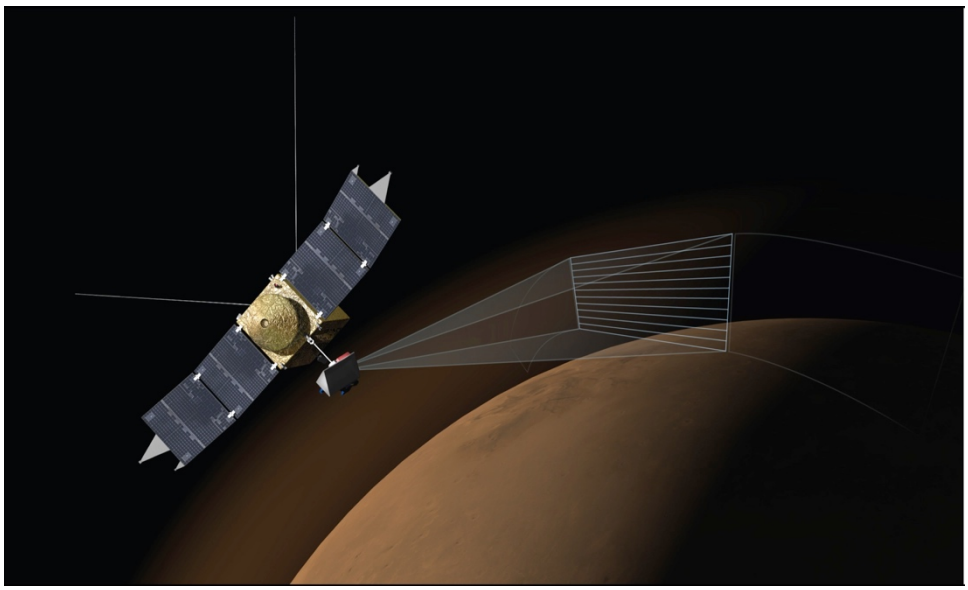

Figure 7: The IUVS scanning the limb of the planet when the spacecraft is in the periapsis portion of the orbit. Figure was obtained from Dr. Nick Schneider, University of Colorado, through personal communication.

As discussed in Chapter 2, the observations from the MUV detector will be used in this study. The spectral information from the MUV detector will provide the necessary information on the CO_2 density in the atmosphere. The spectral information from FUV detector will also be used for the determination of the O/CO_2 ratios which is also described in Chapter 2 in detail.

1.6 NGIMS

The Neutral Gas and Ion Mass Spectrometer (NGIMS) as described in (Mahaffy et al., 2015), is a quadrupole mass spectrometer used to make *in situ* measurements of densities between 2 amu and 150 amu with a unit mass resolution. The density of neutral species such as Ar, CO_2, N_2 and He is measured during every orbit when the spacecraft is below ~500 km altitude. The reactive species such as O, CO and NO and the ions are measured in alternate orbits.

The analysis shown in this thesis using the NGIMS data is done by Dr. Guiping Liu (Researcher, Space Sciences Laboratory, UC Berkeley). The initial interest in this project arose from Dr. Liu's analysis of the NGIMS data during March-April 2016 which showed a structure in the densities that could be attributed to atmospheric tides. Part of the work done in this thesis is to validate these structures seen by NGIMS, using the remote sensing observations obtained by the IUVS.

1.7 Tides observed by MAVEN

Atmospheric tides have been observed using observations from the MAVEN spacecraft. This section presents a summary of all previous results that have been reported, based on observations

from MAVEN.

Non-migrating tides were first observed near the equator with a strong wave number 2 component using the IUVS (Lo et al., 2015). The CO_2^+UVD emission measurements taken by the IUVS were used as a proxy for CO_2 density and to subsequently identify the perturbations in these densities. The dominance of wave number 2 near the equator is characteristic of the diurnal eastward tide (DE1), also seen in previous observation and modelling results. Although, these results were generally at higher altitudes ~100 – 190 km (Lo et al., 2015) than those in previous observations & results with an altitude of 130 km (Bougher et al., 2001).

Longitudinal variations in the neutral upper atmosphere of Mars associated with non-migrating tides were shown in a first comparative study using both remote sensing and *in situ* observations from the IUVS and NGIMS respectively (England et al., 2016). CO_2^+UVD emission measurements from IUVS were again used as a proxy for CO_2 densities. Analysis of the CO_2 densities from both instruments revealed a strong wave number 2 component in a fixed local time reference frame. Wave numbers 1 and 3 were also present but had much weaker amplitudes. Tidal signatures were also identified in various atmospheric species with NGIMS, including Ar, N_2, He and O. The amplitude of the wave seen in each of those species was different, thereby showing the impact of tides on the composition.

Longitudinal variations in Ar observations are also observed for every month from February to December 2015 with a strong wave number 2 and 3 component (Liu et al., 2017). Since the observations for the months of May and November were at similar latitudes and local times but at different solar longitudes, it enabled a limited study of seasonal impact of tides. The wave number 2 and wave number 3 components dominated the change in mean density with a larger wave number 2 component in the month of November. Relative density variations in CO_2, Ar, N_2, He and O have been shown to change with season having greater wave amplitudes in the month of November than in May, showing the impact of tides on the the composition.

On the other hand modelling results suggest that the observed tidal structures does not move with local time (Medvedev et al., 2016). Comparison of the modeling results is done with the observations from the IUVS data. The dataset was same the one used to identify non-migrating tides by Lo et al., 2015. These results are in contrast to the modeling results explained in section 2.1 where the longitudinal structures are attributed to non-migrating tides (Forbes and Hagan, 2000). On the other hand, these results compliment the longitudinal structures observed using the MGS aerobraking measurements associated with stationary planetary waves (Keating et al., 1998) also explained in section 2.1.

My objective in the coming chapters is to understand the nature of variations in the densities observed in the upper atmosphere of Mars and then to understand the underlying cause of the observed variation. The chapters are structured as follows: Chapter 2 discuses the analysis done and methodology adopted by means of a single control case study – focusing on the time period already documented in (England et al., 2016), but using updated datasets, Chapter 3 discuses the analysis and results for the selected cases, Chapter 4 discuses the conclusions derived from the case studies.

2 Control study

This chapter introduces the data availability, selection criteria for the data, the analysis and methodology that will be used in Chapter 3, by means of a control study. The control study is based on the analysis and results of (England et al., 2016), in which observations of non-migrating tides were reported using the IUVS and NGIMS instruments on MAVEN. This was the first combined study for observations available at the time from both instruments. The results of this paper have been reproduced in this chapter and serves a few purposes 1) the version of software and calibration used to produce the data files as well as their revisions have changed since it was last used in the paper (England et al., 2016). Since strong signatures of tides were observed using the older data files, it is important to confirm that the same features are observed in the new data files and that no drastic changes have been made to the dataset. 2) to ensure the performance and accuracy of codes developed for the analysis.

2.1 $CO_2^+ UV\ doublet$

The observations from the neutral mass spectrometers on Viking 1 and 2 established that CO_2 was the most abundant constituent in the upper atmosphere of Mars (A. O. Nier and M. B. McElroy, 1976). Airglow in the Martian atmosphere emerges due to the interaction of solar ultraviolet radiation with CO_2. The $CO_2^+ UV\ doublet$ is one of the well studied features of the Martian dayglow and was first observed during the Mariner 6 mission by Barth et al., 1971. $CO_2^+ UV\ doublet$ is the second brightest emission in the atmosphere of Mars. This can be seen in the ultraviolet emission spectra of the dayglow of Mars as shown in Figure 8.

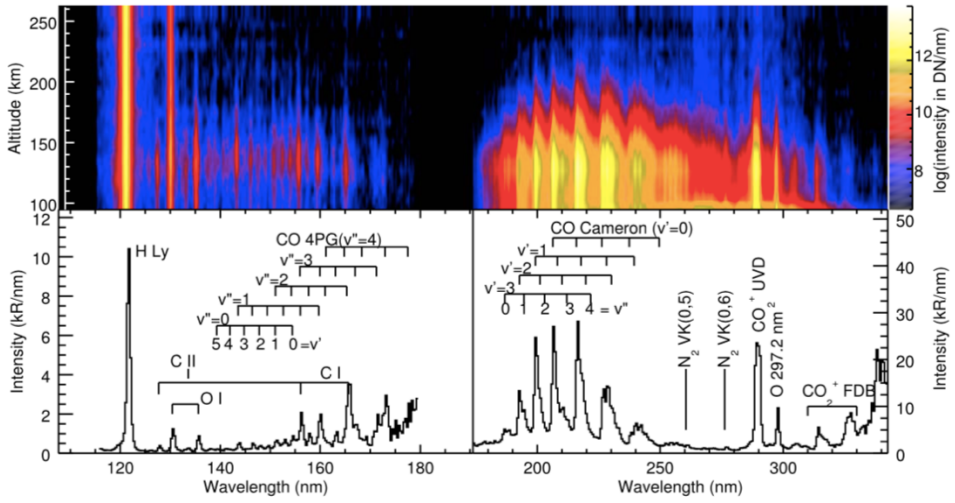

Figure 8: The ultraviolet dayglow spectrum of the upper atmosphere of Mars. Figure from (Jain et al., 2015). The spectrum on the bottom left is derived from the far ultraviolet (FUV) detector and that on the bottom right is derived from the middle ultraviolet (MUV) detector. The $CO_2^+ UV\ doublet$ emission feature can be distinctly identified at ~289nm in the MUV spectra. The top panel is a wavelength-altitude image produced by using the FUV and MUV detectors from a single vertical scan of orbit 110. The color in the top panel denotes the signal intensity at each altitude / wavelength measured in units of digital numbers/nanometer.

Almost all of the molecular emission and some of the atomic emissions "may be and probably are produced due to the action of solar photons and photoelectrons on carbon dioxide" (Barth et al., 1972). The dominant process responsible for the production of the UV doublet is photoionization (Barth et al., 1972). As described in Stiepen et al., 2015 the $CO_2^+ UV\ doublet$ emission is produced by the de-excitation of CO_2^+ ions in the $B^2\Sigma^+$ state to the $X^2\ \Sigma^+$ state. The $CO_2^+\ (B^2\Sigma_u^+)$ emission is a result of photoionization or photoelectron impact or fluorescent scattering of CO_2. The transitions for each of the above mentioned mechanisms are shown below.

Photoionization: $CO_2 + h\nu\ \rightarrow CO_2^+(A^2\Pi_u, B^2\Sigma_u^+) +\ e^-$

Photoelectron impact: $CO_2 + e^-\ \rightarrow CO_2^+(A^2\Pi_u, B^2\Sigma_u^+) +\ 2e^-$

Fluorescent scattering: $CO_2^+(X^2\Pi_g)\ \rightarrow CO_2^+(A^2\Pi_u, B^2\Sigma_u^+)$

The major factors controlling the CO_2^+ volume emission rates are the densities of CO_2, the UV insolation incident on the upper atmosphere and the photoelectron flux. This dayglow feature can be used to represent the bulk neutral densities of CO_2 in the thermosphere (Fox and Dalgarno, 1979; Jain and Bhardwaj, 2012).

The use of $CO_2^+ UV$ doublet as a proxy for CO_2 densities has been demonstrated in previous studies (England et al., 2016; Lo et al., 2015). As shown in Figure 8, the IUVS MUV detector image shows the distinct UV doublet emission feature. The altitude profiles of this emission feature will be used to infer the perturbations in CO_2 densities. The tidal features can then be identified using density perturbations of CO_2.

It is important to note that the Martian nightglow does not consist of an equivalent emission feature that can be used to represent the neutral density, therefore the data used in the study is limited to the observations taken when the limb of the planet during spacecraft periapsis is sunlit (England et al., 2016).

2.2 Data availability and selection

Following the description in (England et al., 2016), the selection of data is governed by the fact that this is a comparative study which uses observations from both the IUVS and NGIMS instruments. It is therefore essential that the time period or date range of the data used for analysis include data from both instruments that generally overlap. However, perfect overlap is not possible due to constraints on the measurements taken by the instruments. IUVS makes its observations only when the solar zenith angle is below 80°. There is no data available from IUVS during conjunction i.e. when the Earth, Sun and Mars align with the Sun in between, this is because of the excessive radio interference from the Sun. And lastly there is no the data from IUVS during its deep dip campaigns (DD1, DD2 etc.), as the spacecraft dips very low in altitude and does not satisfy the orbit geometry conditions required for the limb scan observations. These constraints can be visualized in Figure 9 which displays the plot of the solar zenith angle in purple-orange and the orbit evolution of NGIMS instrument in green - yellow.

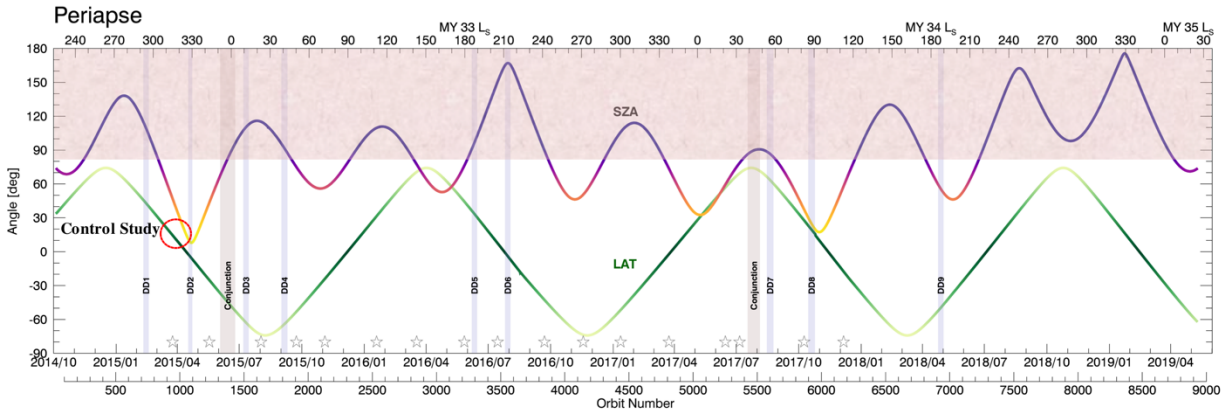

Figure 9: Shows the solar zenith angle in purple-orange and the NGIMS orbit in green-yellow. The portion highlighted in dark gray rules out solar zenith angles greater than 80° with no data from the IUVS. The DD1, DD2 and so on highlighted in light gray indicate the deep dip campaigns, and lastly conjunctions highlighted in gray-yellow.

The best available observations are used to identify the signatures of tides. The data obtained during a single orbit cannot be utilized since IUVS scans the limb of the planet with its line of sight oriented perpendicular to the radius vector of the planet, whereas NGIMS makes measurements in the ram direction or in other words, along the direction of the spacecraft velocity vector. As a result of IUVS and NGIMS making observations at different locations, the few degrees of separation in these observations is translated into a local time difference. The local times observed by both instruments will therefore differ by ~1hr. However, this will not pose as a problem since the period of the tides that are anticipated based on previous studies is either 12 hr or 24 hr, hence the difference in local time will present itself as a small phase difference in the tides observed by both instruments within the same date range. For conducting the analysis of atmospheric tides, complete longitudinal coverage is required and therefore the data from multiple orbits of both instruments are used.

The following subsections will describe the datasets used and the selection criteria for analysis.

2.2.1 IUVS data

The IUVS software interface specification describes the organization of the dataset based on different levels of processing. The level one (L1C) data files contain the calibrated brightness of the observed spectral features. The spectral features in the emission spectra are isolated and binned spatially on an altitude grid. The data files used in (England et al., 2016) is version 2 revision 1 (v02r01), whereas the control study uses version 07 r01 (v07r01). It is useful to note that change in versions indicate change in software which can result in additional quantities included in the dataset, whereas change in revisions indicate reprocessing of data due changes in calibration of the instrument or bug fixes.

The IUVS data used in this study is obtained during the periapse portion of the orbit i.e. when the spacecraft is below ~500 km altitude. As mentioned in section 1.5, 12 scans are performed in each orbit. The date-range chosen based on availability and overlap with the NGIMS spans from from April 1st to 3rd of 2015. The analysis for this time period includes 13 orbits ranging from orbit 973 to orbit 986 (England et al., 2016). The emission altitudes of the $CO_2^+UV\ doublet$ determine the

altitude range of the observations. The tangent point location range for the control study is selected to be between 160 km and 200 km.

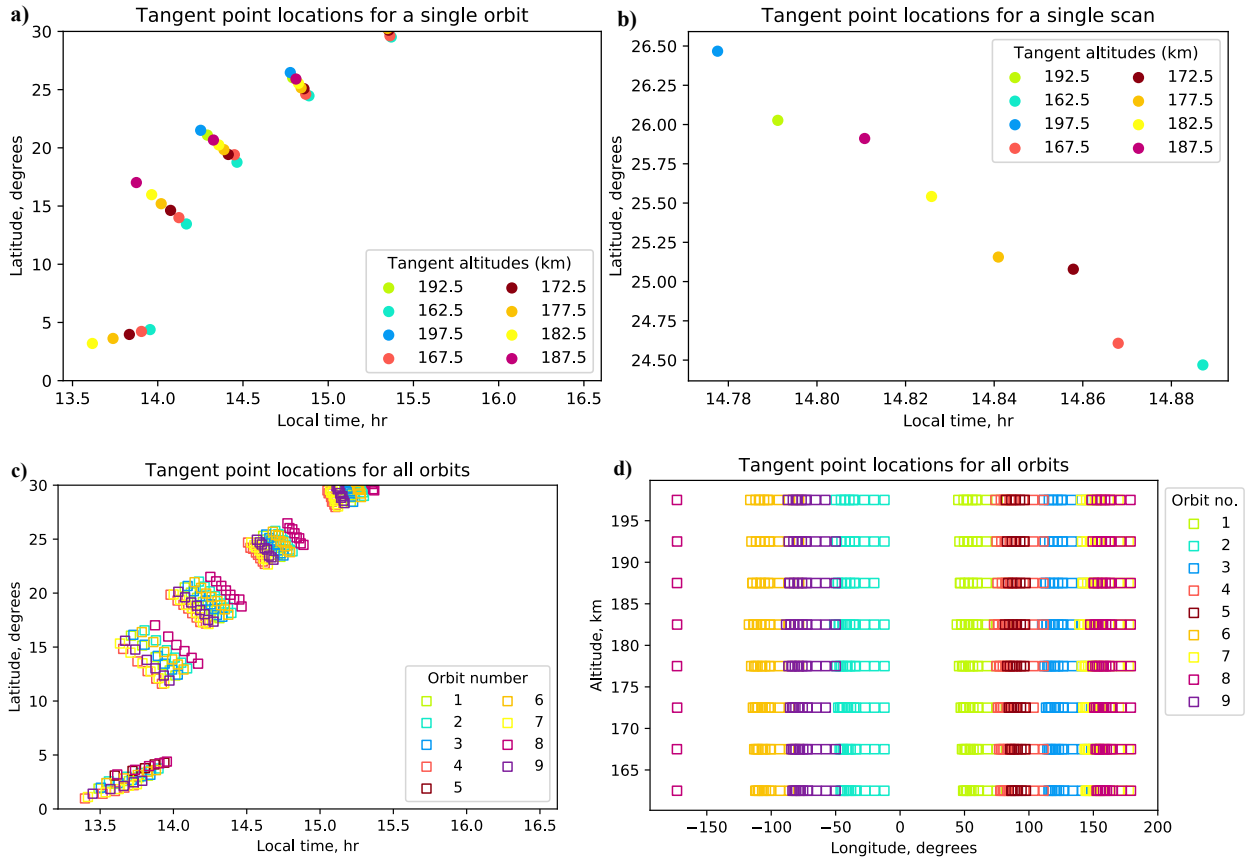

Figure 10: a) The tangent point locations as a function of latitude and local time for a single orbit. b) shows the tangent point locations of just one scan. c) shows the tangent point locations from all the orbits used in the analysis. d) Shows the tangent point locations of all the orbit similar to c) but as a function of longitude and altitude.

Figure 10a shows the range of tangent point altitudes between 160 km and 200 km plotted as a function of latitude and local time for a single orbit. The near-equator latitudes are chosen based on observations of non-migrating tides in this region (Lo et al., 2015). A single orbit thus consists about 5 scans for the selected latitude range. A closer look at the scan is shown in Figure 10b where the observations are taken at the tangent point altitudes. Figure 10c shows the observations from all the orbits with each color representing the tangent point locations from a particular orbit. The clustering of data points is due to observations from multiple orbits being considered. Figure 10d shows that observations from multiple orbits provides complete longitudinal coverage which is required for the analysis of tides. Observations from 9 out of the 13 orbits can be seen in this figure. The remaining orbits did not fall into the criteria used to choose the tangent point locations.

2.2.2 NGIMS data

The main sources for the description in this section are (England et al., 2016) and (Mahaffy et al., 2015). The NGIMS is a quadrupole mass spectrometer and operates with a unit mass resolution. The spectral range measured by NGIMS is 2 – 150 AMU. The NGIMS data used in the control

study is the Level 2, version 5, revision 1 data. This dataset consists the number densities of the various species measured by the NGIMS.

It is useful to note that there is no NGIMS data prior to the deep dip 1 campaign (DD1). And hence the data from February 2016 to April 2016 is considered. As mentioned previously, the NGIMS analysis is done as part of a collaborative effort. The NGIMS data and results discussed hereafter has been directly extracted from (England et al., 2016).

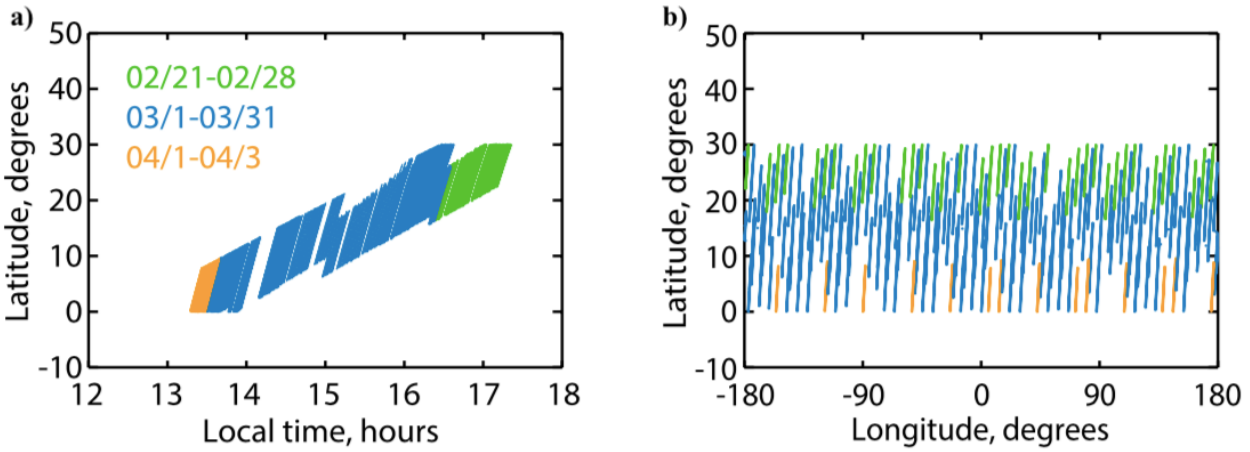

Figure 11: Plots from (England et al., 2016) of the location and coverage of the NGIMS dataset used in the control study. Figure 4a shows that the for the NGIMS observations the local times and latitudes cannot be separated for the specific period of observation.

The NGIMS data distribution can be visualized in Figure 11 from (England et al., 2016), where Figure 11a, show that the coverage obtained is in the same latitude range as that by the IUVS between 0 to 30°. Figure 11b shows that over the selected date range there is sufficient longituinal coverage as well.

2.3 Analysis and Methodology

The IUVS measures brightness along the line of sight. The observation location is where the ray path becomes parallel to the surface also called the 'tangent point'. The tangent point is chosen because it has the longest path length and therefore can be assumed to have the maximum contribution of light. As mentioned in section 1.5, the limb of the atmosphere is scanned during periapsis. A single complete scan is made by the scan mirror moving the field of view vertically to sample different tangent altitudes. The altitude range covered by the IUVS scans during periapsis is between 100 and 225 km (McClintock et al., 2015).The spacecraft motion between two scans is considerably greater than the spacecraft motion within a scan. This is can be seen in Figure 10a.

In order to identify the tidal components, the data must be grouped into spatial bins. The brightness and longitudes are extracted based on the tangent altitude, tangent latitude and local time range. This brightness data is then grouped into 10 km altitude, 10° latitude and 30° longitude bins respectively. When binning data, we use the profile tangent altitudes, tangent latitude, tangent longitudes and local times provided in the L1C data set. As mentioned in section 2.1, only

observations from the day time can be utilized, the data points chosen are therefore between local times 13.5 hr and 16.5 hr. Since we do not know the period of the tide prior to analysis, the biggest sample that could be considered is 4 hours. The $CO_2^+UV\ doublet$ emission peaks at around 130 km with negligible emissions above 200 km. This constrains the upper and lower limits of the emission altitudes for the analysis. The 10° latitude bins are chosen because a smaller bin width would result in insufficient data points per bin. This can be seen in Figure 10c where there is a gap in the data between 5° and 10°. The smallest tidal component expected to be identified is the wave number 3 which has a phase of 120°. The 30° longitude bin is thus sufficiently smaller than the wave number and smaller than the variations expected every 120°. The vertical resolution of the IUVS for the limb scans is ~5 km. The altitudes are therefore grouped in 10 km altitude bins since this is lesser than the scale height of CO_2 which is ~11 – 16 km (England et al., 2017). Since the distribution of data points in altitude is not the same, the bin is made smaller than the e-folding distance. This ensure sufficient data points per bin.

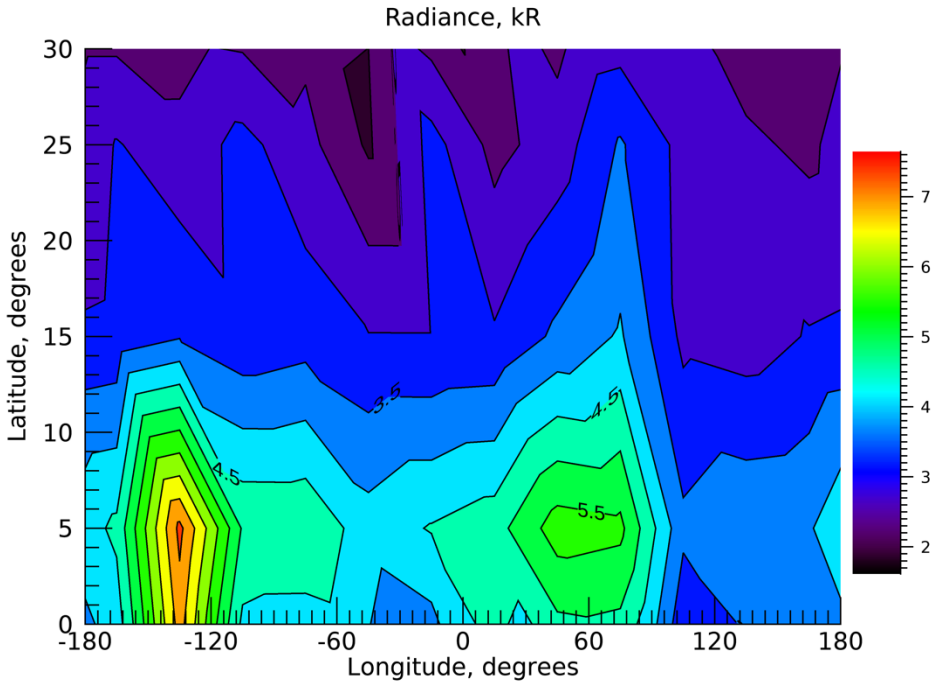

Figure 12: A plot of mean brightness as a function of latitude and longitude averaged over an altitude range of 160 km - 200 km.

The brightnesses and altitudes are then averaged over each latitude and longitude bin. Figure 12 shows this mean brightness as function of latitude and longitude. A clear structure with two peaks can be identified from this plot.

2.3.1 Conversion of Brightness to Volume Emission Rates

The line of sight brightness is attributed to a particular tangent point altitude, where the signal is heavily weighted to the tangent point. The attribution of the line of sight to the tangent point is an

approximation. The light observed from any line of sight is dependent not only on the brightness at that particular altitude but on all altitudes above that point. The lower we go in altitude the more significant this dependence. The true brightness observed from a particular tangent altitude compared to that of the altitudes above it depends on the tangent point altitude, the brightness profile and spacecraft altitude. To overcome this problem and attribute the brightness to a particular location the volume emission rates are calculated using a simple Abel inversion assuming a spherically symmetric atmosphere.

The method followed to calculate the volume emission rate is a simple Abel, or onion peeling inversion. The atmospheric region of interest is divided into vertical shells of uniform thickness of 5 km and each shell is assumed to be horizontally homogenous. The thickness of the layer is chosen to be smaller than the scale height which is ~11-15 km as well as big enough to cover sufficient data points for analysis. Given that the thickness of each layer is 5 km, the total number of layers are found by using the altitude range of interest. The ray of known path length that crosses the topmost layer is utilized to yield the volume emission rate for that particular layer. For the layer immediately below the topmost layer, the volume emission rates for both layer 1 (topmost) and layer 2 (the current layer of interest) are required to be known. The volume emission rate for layer 2 is solved for using the known volume emission rate for layer 1.

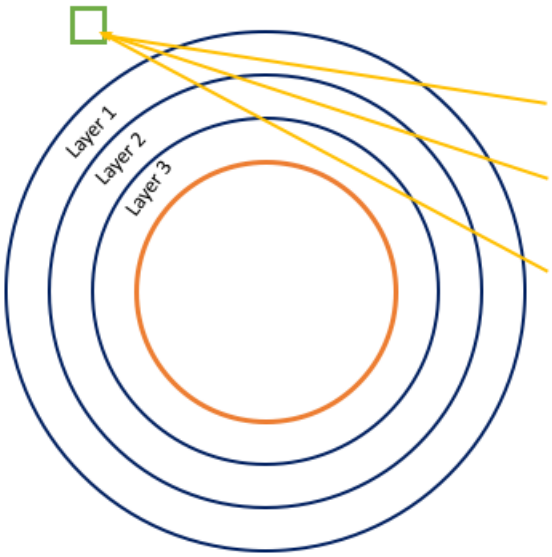

Figure 13: Figure of limb viewing from satellite and onion peeling geometry.

The conversion of brightness to volume emission rates have been performed using Dr. Scott England's code, used in (England et al., 2016). These volume emission rates are then binned in the same manner as the brightness data. The mean volume emission rate is then calculated for each latitude-longitude bin averaged over all altitudes i.e. between 160 – 200 km. The plot for the mean volume emission rates is shown in Figure 14.

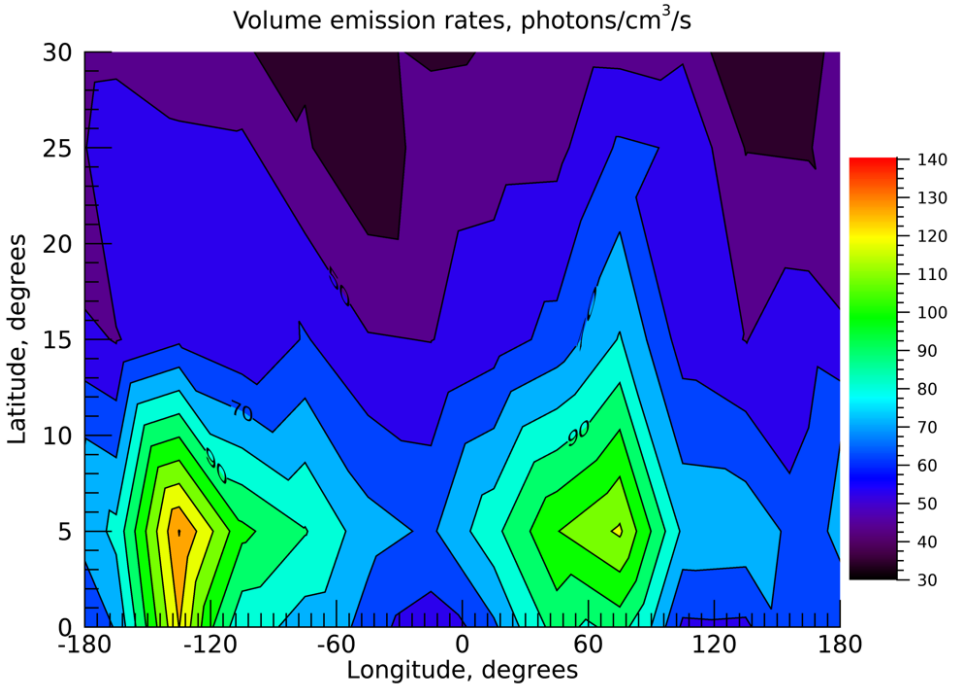

Figure 14: The mean volume emission rates as a function of latitude and longitude averaged over 160 - 200 km altitude range. The plot uses the L1C v07r01 data.

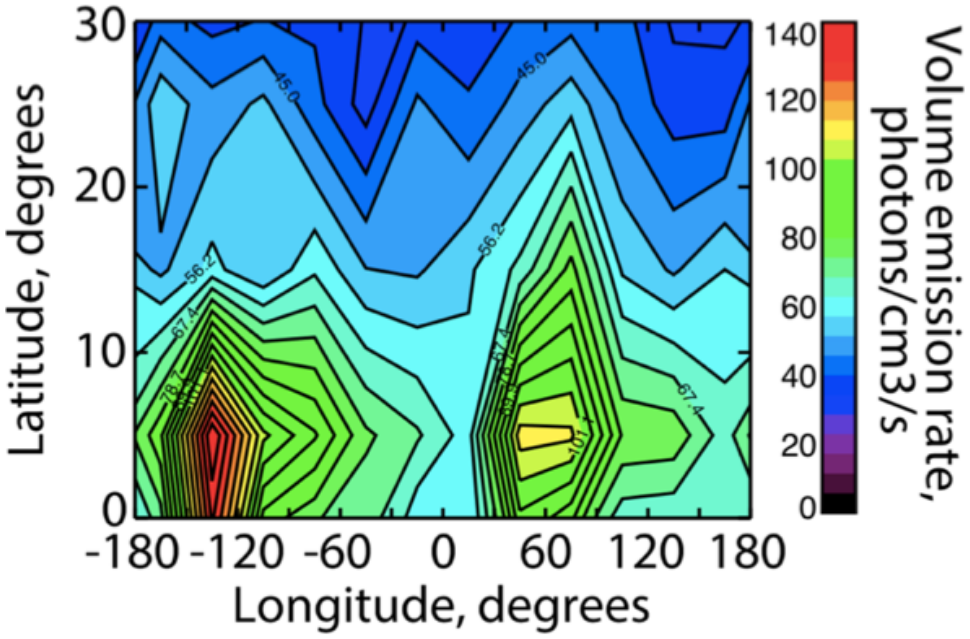

Figure 15: Plot of the mean volume emission rates as a function of latitude and longitude from England et al., 2016, using the L1C v02r01data.

This plot was obtained by processing the L1C v07r01 data and can be compared to the mean volume emission rate plot from (England et al., 2016) which used the L1C v02r01 shown in Figure 15 for the same date range, altitude range, latitudes and local times. Hence, the same selection criteria were used to obtain the results from both datasets. Both plots strongly agree showing two prominent peaks centered around -130° and 70° longitude respectively with a stronger peak at -130°. The calculated values of the volume emission rates also show a strong agreement and can be compared by the values displayed on the colorbars accompanying the plots. The subtle differences in the plots are attributed to change in versions of the dataset, but there is a general agreement which establishes that tidal analysis can be performed for the revised datasets.

2.4 Densities and Temperatures

In addition to L1C data, the analysis has been taken a step further and the level 2 (L2) files which contain the derived densities have been analyzed. The IUVS L2, version 7, revision 1 files used here are available on the Planetary data system (PDS) at https://pds.nasa.gov. The L2 files are produced by converting the distinct emission features to density profiles. The densities are calculated taking into account the variations in the solar input, whereas the calculation for the volume emission rates assumes constant insolation with negligible fluctuations in solar influx. This assumption works well for the control study since it spans a date range of four days in the case of the IUVS data. The results expected from the densities is a structure similar to the one observed in the volume emission rates.

The methodology adopted here is the same as that for the brightnesses and volume emission rates. The Figure 16 shows the mean densities as a function of latitude and longitude averaged over 160 – 200 km. It can be seen that there are data gaps in this plot, which is due to the fact that only four days of data has been analyzed and hence there are insufficient data points. Although, looking closely it could be said that there is a strong feature at ~70°. In order to fill in the data gaps, the mean of the densities in each latitude bin was calculated. This value was used to replace the missing data points in each corresponding latitude bin. This is not a replacement for actual data values, but aids only in visual identification of structures, and cannot be used for a quantitative assessment.

Figure 17 shows the plot of this modified mean densities. The plot clearly shows two features, similar to the previous plots for the VER's. The intensity of the feature centered around -100° is unclear and cannot be determined. This feature is also not as strong as observed in the VER's whereas the feature centered around 70° is more prominent compared to the VER's.

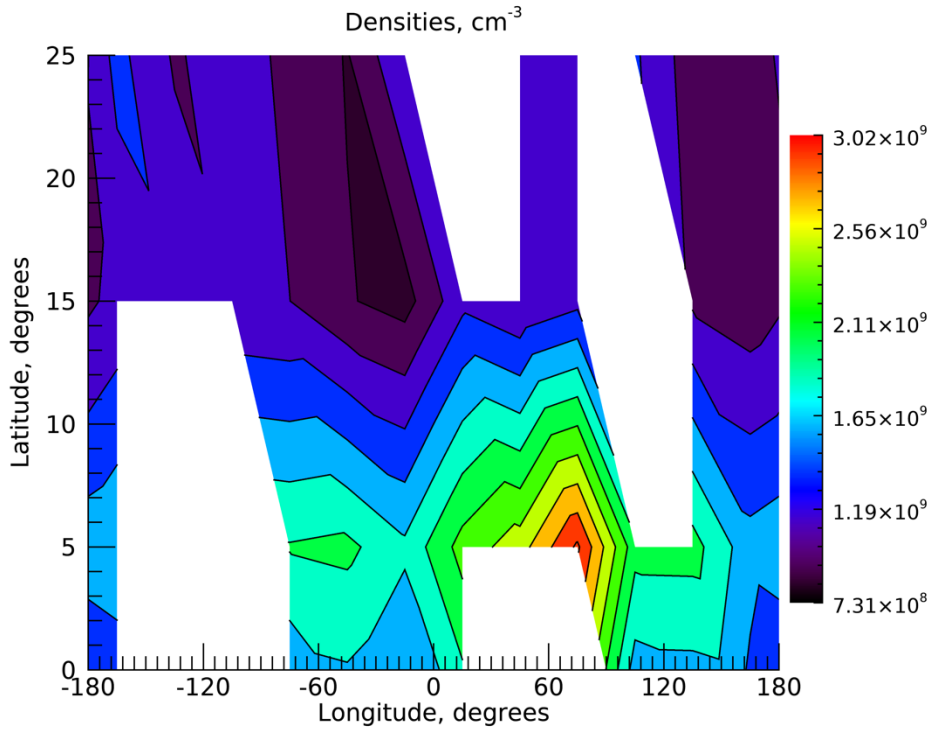

Figure 16: Plot shows the mean densities as a function of latitude and longitude averaged over the tangent altitudes between 160 and 200 km.

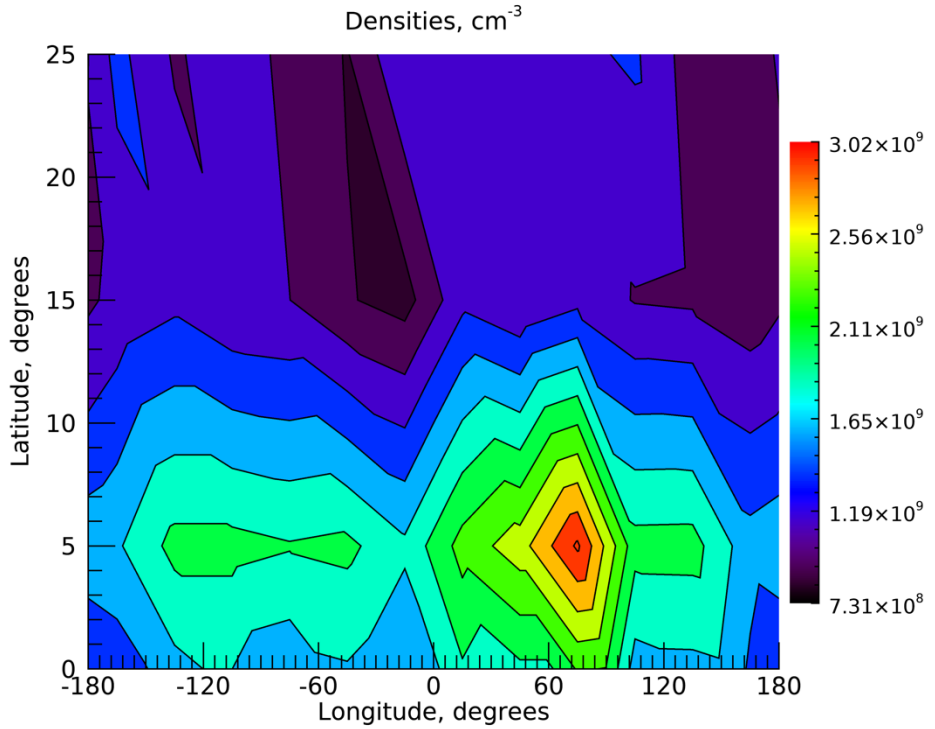

Figure 17: Plot of the mean densities similar to Figure 16 with data gaps filled in using the average densities in each latitude bin.

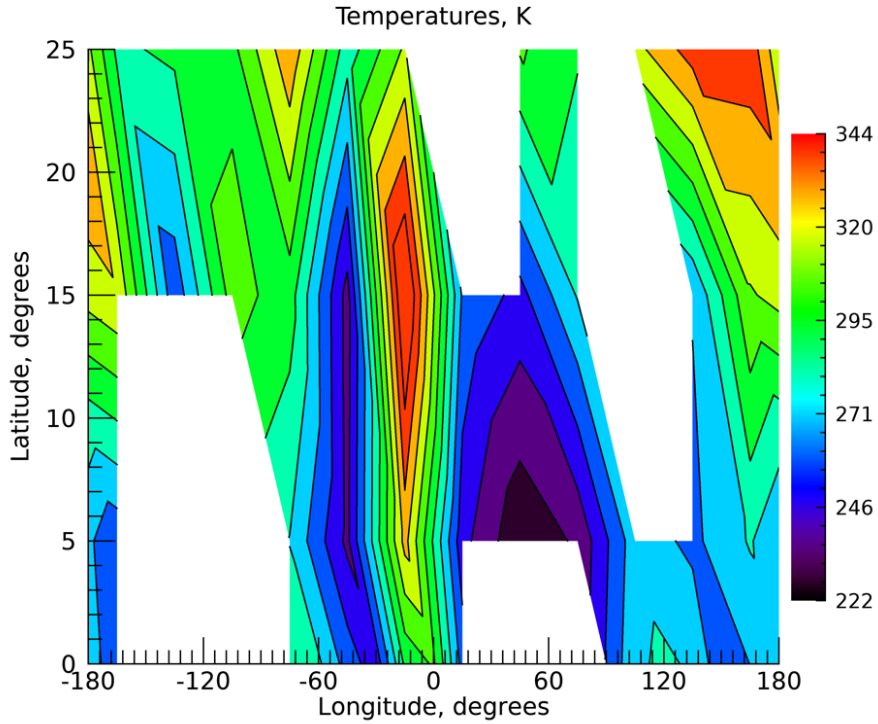

Figure 18: Plot shows the mean temperatures as a function of latitude and longitude averaged over the tangent altitudes between 160 and 200 km.

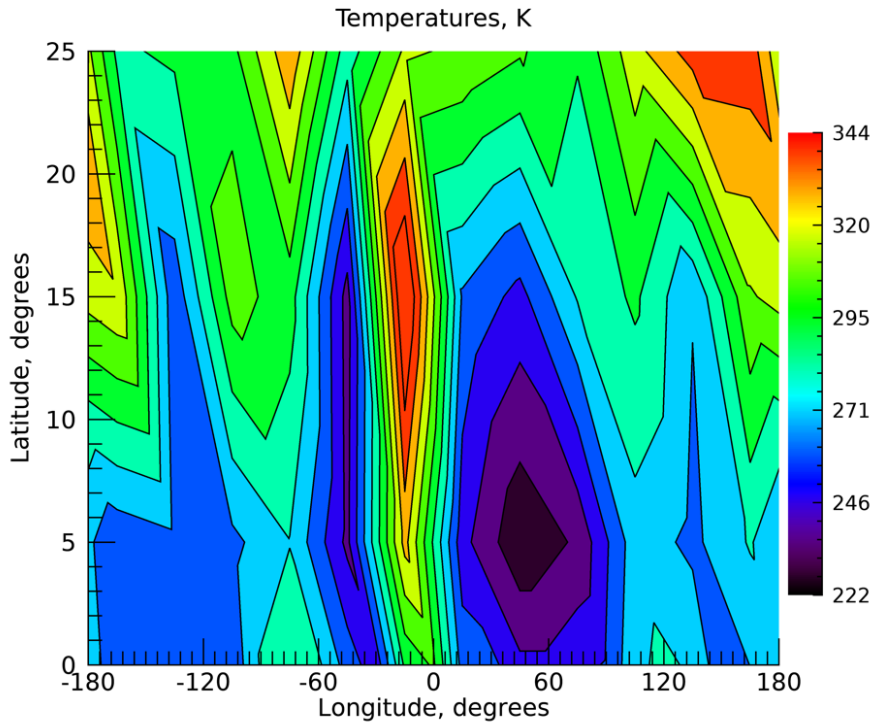

Figure 19: Plot of the mean temperatures similar to Figure 18 with data gaps filled in using the average temperatures in each latitude bin.

Figure 18 shows the plot of the mean temperatures as a function of latitude and longitude. The temperature profiles have a 1:1 ratio with the density profiles and are binned on the same altitude grid, hence share the same missing data points. The same method is used to fill the data gaps as with the densities. The plots show a clear anti-correlation with the densities.

By applying the linear wave theory for inertia gravity waves, when the densities are high the temperatures must be low and vice versa. This can be inferred from Figure 20 where the densities ($\rho < 0$) are out of phase with the temperatures (WARM). The temperatures in Figure 19 seems to follow this theoretical conclusion thereby further validating that the density perturbations observed are due to tides.

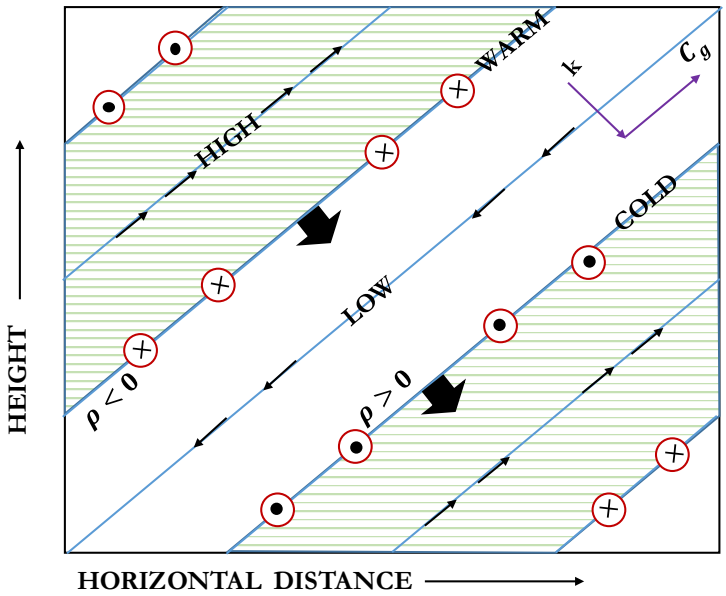

Figure 20: Vertical section of a wave adapted from Andrews et al., 1987 in the plane of the wave vector k. The arrows coming into and out of the page indicate the velocity vector components. The thick black arrows indicate the direction of propagation of the phase of the wave. The pressure is indicated by the words "HIGH" and "LOW" whereas the temperatures are indicated by the words "WARM" and "COLD".

2.5 Wavefits

In order to characterize the structure observed in the analysis conducted above, wavefits are performed over the volume emission rates at latitudes where the perturbations are observed. The code for performing the wavefits is borrowed from Dr. Paul D Withers, and described in (Withers et al., 2003). The code performs a simple least squares fit to the data using a set of superimposed harmonics and a mean value. This fitting method is adopted since it utilizes the uncertainty of the individual measurements by taking into consideration the spread in the data, rather than the stated uncertainties in each datapoint, which is generally much smaller than the variability in the atmosphere itself. The uncertainty found from this method is also recorded, and used to estimate ±1standard deviation above/below the least-sqaures fit, shown in Figure 21.

Figure 21 displays the results of this fit done at various latitude bins. It is clear that the wave number 2 is the dominant wave observed at all three latitude bins considered here. The wave number 2 refers to a wave that varies every 180° (two peaks per 360° longitude), similarly wave

number 3 varies every 120° (three peaks per 360° longitude) and so on. Wave-2 has the greatest relative amplitude of 27.4% centered at 5°.

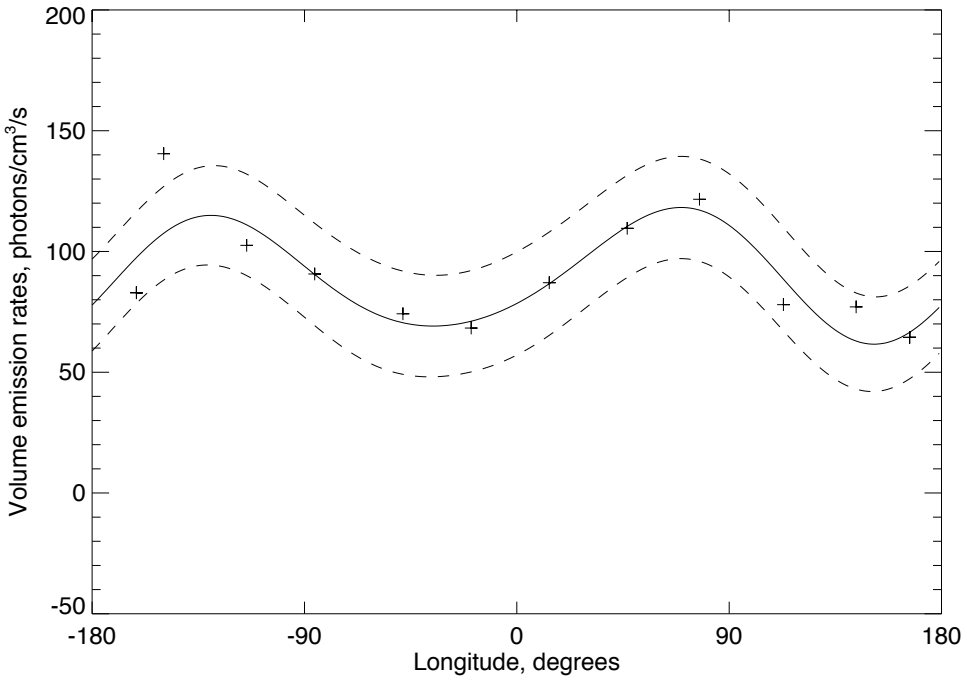

Figure 21: A wave-3 harmonic fit is done to the mean volume emission rates averaged over 160-200 km between 0° and 10N° shown by the solid line. The dashed line shows the 1σ uncertainties about the fit (solid line).

Latitude bins (Centered at)	Relative Amplitude Wave - 1	Relative Amplitude Wave - 2	Relative Amplitude Wave - 3	Phase Wave - 1	Phase Wave - 2	Phase Wave - 3
5°	3.2%	27.4%	6.2%	276.352	59.645	32.232
15°	10.8%	12.6%	6.7%	257.713	79.058	6.871
25°	10.5%	19.8%	10.6%	321.21	55.678	30.019

Table 3: The parameters obtained from the model fit to the calculated volume emission rates for measurements made between 0-10°N, 10-20°N and 20-30°N.

The wavefits 1 through 3 done for the volume emission rates derived from the older data in (England et al., 2016) is shown in Figure 22. The amplitudes shown here are percentages with respect to the mean zonal volume emission rate. As can be seen the wave number 2 varies between ~13.5% to 29%, with 29% at the lowest latitude bin. These amplitudes are very close to those found using the new dataset and can be clearly seen by comparing to the values in Table 3.

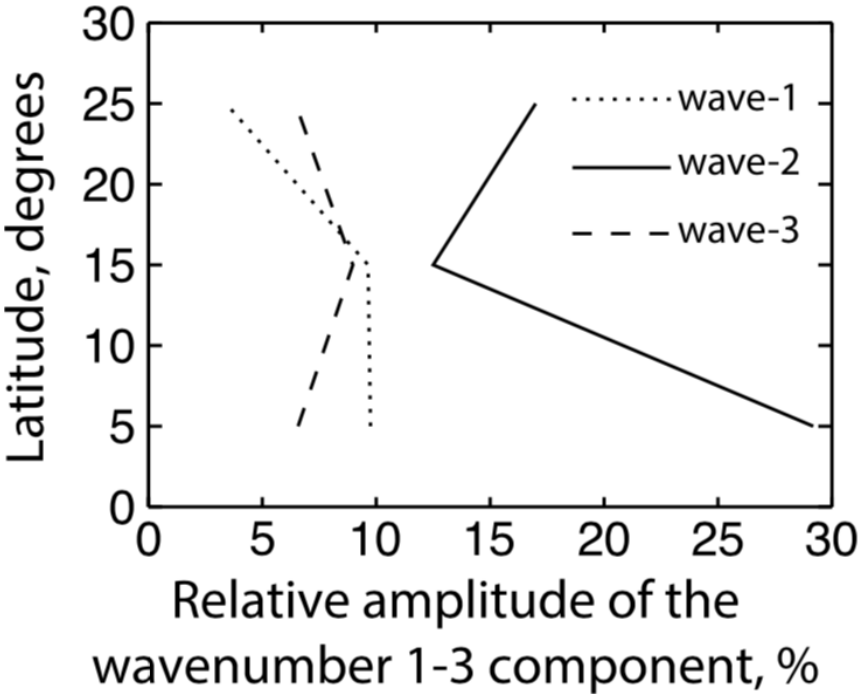

Figure 22: Plot of the wavefits 1-3 from (England et al., 2016). These wavefits were done on the volume emission rate data shown in figure 6b.

2.6 O/CO_2 ratio

The dominant species at the higher altitudes is O whereas the dominant species at low altitudes is CO_2. The upper atmosphere of Mars is mostly made of O^+which is created when O is ionized. Calculating the O/CO_2 helps in determining the amount of O that is available to ionize. The O/CO_2 also enables the measurement of the ratio of molecular oxygen to atomic oxygen. Knowing this ratio has important implications in understanding and controlling spacecraft drag. Since Mars' atmosphere is mostly made up of CO_2 and with O being light, this ratio is also key in estimating the portion of the atmosphere that could escape to space. The O/CO_2 ratio calculated is specific to one location and time, and hence the ratio varies with changes in location or time.

The continuity equation for a linear, plane wave perturbation can be written as:

$$\frac{\tilde{\rho}}{\overline{\rho}} = \frac{i}{\omega}\left(\frac{\widetilde{w}}{H_j} - \nabla.\tilde{V}\right)$$

where $\tilde{\rho}$ is the wave component and $\overline{\rho}$ is the mean value of the density of species given by 'j', ω is the wave frequency, $\widetilde{w}$ is the vertical velocity distribution, H_j is the species dependent scale height, $\tilde{V}$ is the velocity perturbation (England et al., 2017). This equation describes the relation between the vertical winds and the density perturbation. For large scale waves (longer wavelengths), the first term of this equation becomes dominant where it can be seen that the density perturbations vary with respect to the inverse of the scale height of the particular species.

The O/CO_2 ratio calculated using the the NGIMS data shows a variation of about 24% between the regions of maximum and minimum densities (England et al., 2016). There is not sufficient density data from the IUVS within the time period chosen to calculate this ratio, but it will be

calculated in Chapter 3 for the new cases considered for analysis.

2.7 Comparison with the NGIMS results

The NGIMS results from (England et al., 2016), are shown in Figure 23 and Figure 24. Figure 23 shows the mean densities plotted as a function of altitude and longitude. The densities are averaged over 0° – 30° in latitude. The plot shows two peaks centered around -130° and 70°. The peaks observed in Figure 14 of the IUVS results are in the same locations.

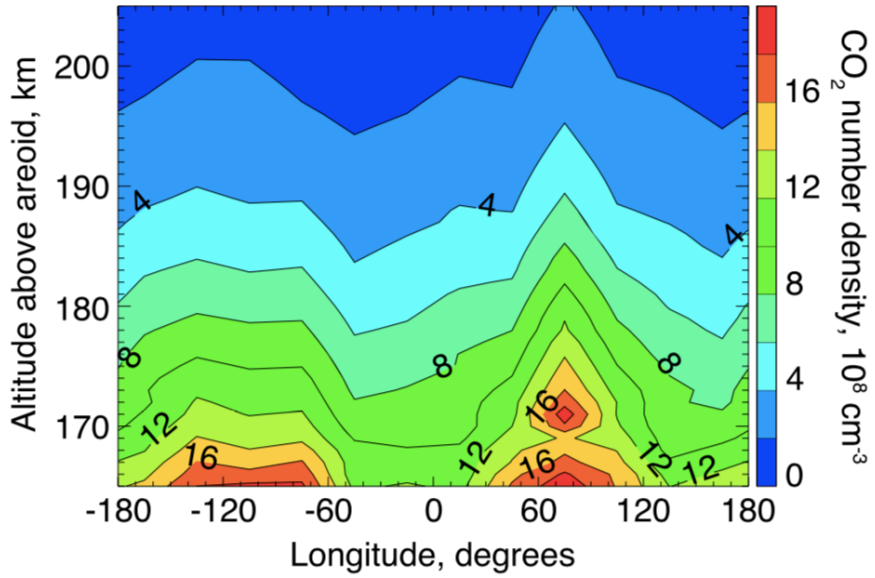

Figure 23: Plot shows the mean densities averaged over 0° to 30°latitude as a function of altitude and longitude from England et al., 2016.

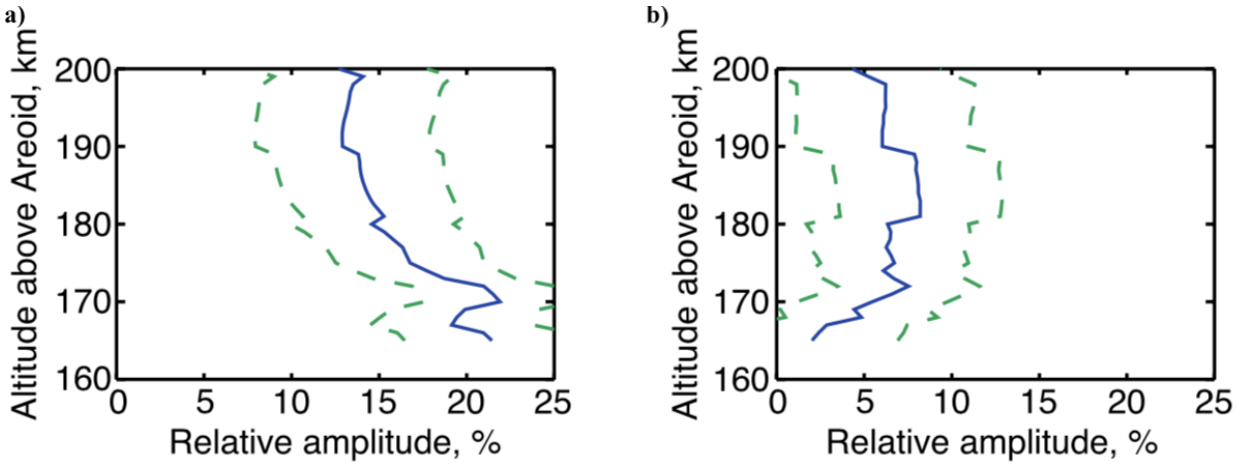

Figure 24: Plots from England et al., 2016 figures 4b and 4c of the wave fits 2 and 3 on the mean CO_2 densities obtained from NGIMS.

The wave fits 2 and 3 from figures 4b and 4c of (England et al., 2016) is shown in the Figure 24. These wave fits were done on the NGIMS CO_2 density data shown in Figure 23. Figure 24a shows wave number 2 whose relative amplitude varies between ~12.5% to 22% and wavenumber 3 shown in Figure 24b varies between ~2% to 8%. The NGIMS results have a good agreement with

the IUVS results and can be seen by comparing these values to those found in Figure 24 and Figure 22.

2.8 Conclusions for the control case

There is a fairly good agreement by both the IUVS and NGIMS of a strong wave number 2 based on the observations. The IUVS analysis enabled the observation of latitudinal variations in the amplitude of the tide whereas the NGIMS allowed for altitudinal variations to be observed. Non-migrating tidal signatures observed in the control study are near equatorial latitudes and in a fixed local time reference frame.

Ideally, the L2 densities would be considered for the tidal analysis since it accounts for any variation in insolation as well as variations in geometry of the spacecraft. From the control study it is evident that more than four days of data from IUVS would be required for this to be possible to avoid data gaps. Also, the NGIMS observations from a single orbit is dominated by small scale waves (have smaller wavelengths or in other words, the spatial scale is small). Since this study does not focus on these types of waves, it necessitates the averaging of many days of NGIMS data to unambiguously identify the tides. The above two reasons combined make it necessary to use data over multiple orbits and that spans between 3 to 4 weeks. The data for the other cases considered in this study is at higher latitudes. The observations from high latitudes enables the study of tides with variation in local time.

3 Results

The requirements and constraints described in Chapter 2 define the three cases chosen for further study in this chapter. The focus in this analysis is on local time variations of tides with the NGIMS observations. As a result of the MAVEN orbit, this kind of analysis can be done only at higher latitudes. The time periods selected are marked in solid red circles shown in Figure 25.

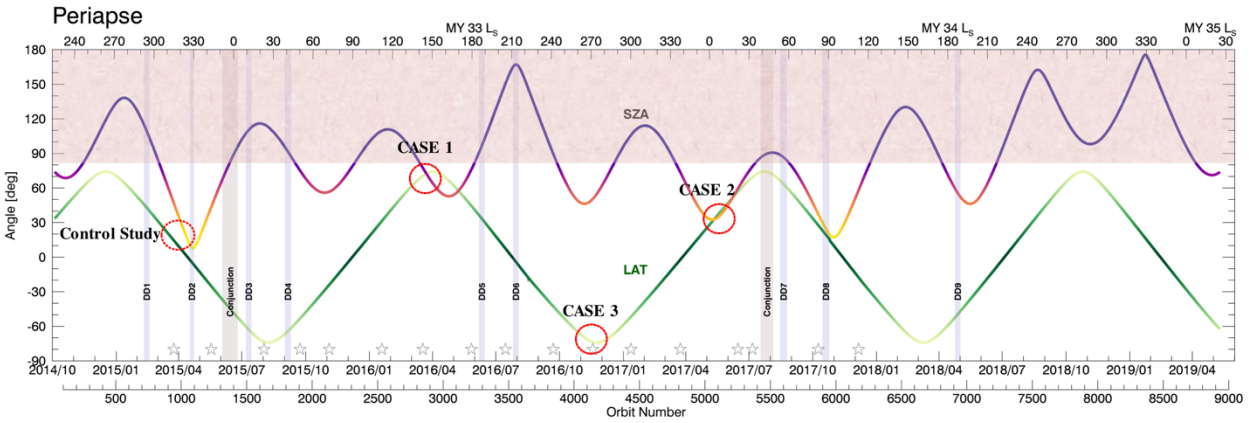

Figure 25: Shows the solar zenith angle in purple-orange and the NGIMS orbit in green-yellow. The portion highlighted in dark gray rules out solar zenith angles greater than 80° with no data from the IUVS. The DD1, DD2 and so on highlighted in light gray indicate.

The non-migrating tides observed are expected to have a time period of either 12 hours or 24 hours. Wave-3 oscillations associated with non-migrating tides were observed at high northern latitudes (Bougher et al., 2001). Density perturbations were observed using two measurements that were 12 hours local time apart in (Bougher et al., 2001), thereby indicating that the underlying cause could be a semi-diurnal tide. Modelling studies further suggested that the density perturbations observed for the same set of observations could be attributed to either a 12 hour tide or a stationary wave (Bougher, 2004).

In this chapter, observations made by the IUVS will be used to identify tidal features using the CO_2^+UVD emission features. Additionally, the IUVS enables the use and analysis of the temperatures and O/CO_2 ratios which will further evidence the tidal observations. Sections 3.1, 3.2 and 3.3 will each describe the data used in Cases 1, 2 and 3 respectively as well as the results obtained by applying the same analysis and methodology as done for the control study. Each will be compared to results determined independently from NGIMS, using analysis provided by Dr. Guiping Liu from the University of California Berkeley.

3.1 Case 1: March and April 2016

3.1.1 Data selection and availability

Case 1 includes data from orbit number 2867 to orbit number 3005. This dataset covers date ranges that fall between the 21st of March 2016 to the 15th of April 2016. Distribution of data for March and April 2016 is shown in Figure 26c. The figures show tangent point locations of the IUVS limb

observations when the tangent point is between 130 and 180 km. The tangent points are shown as a function of latitude and local time. The best overlap in latitudes for the IUVS and NGIMS was found to be when the local times lie between 13 and 17 hours. Since the period of the tide is unknown prior to the analysis, the biggest sample that could be considered is ~3-4 hours.

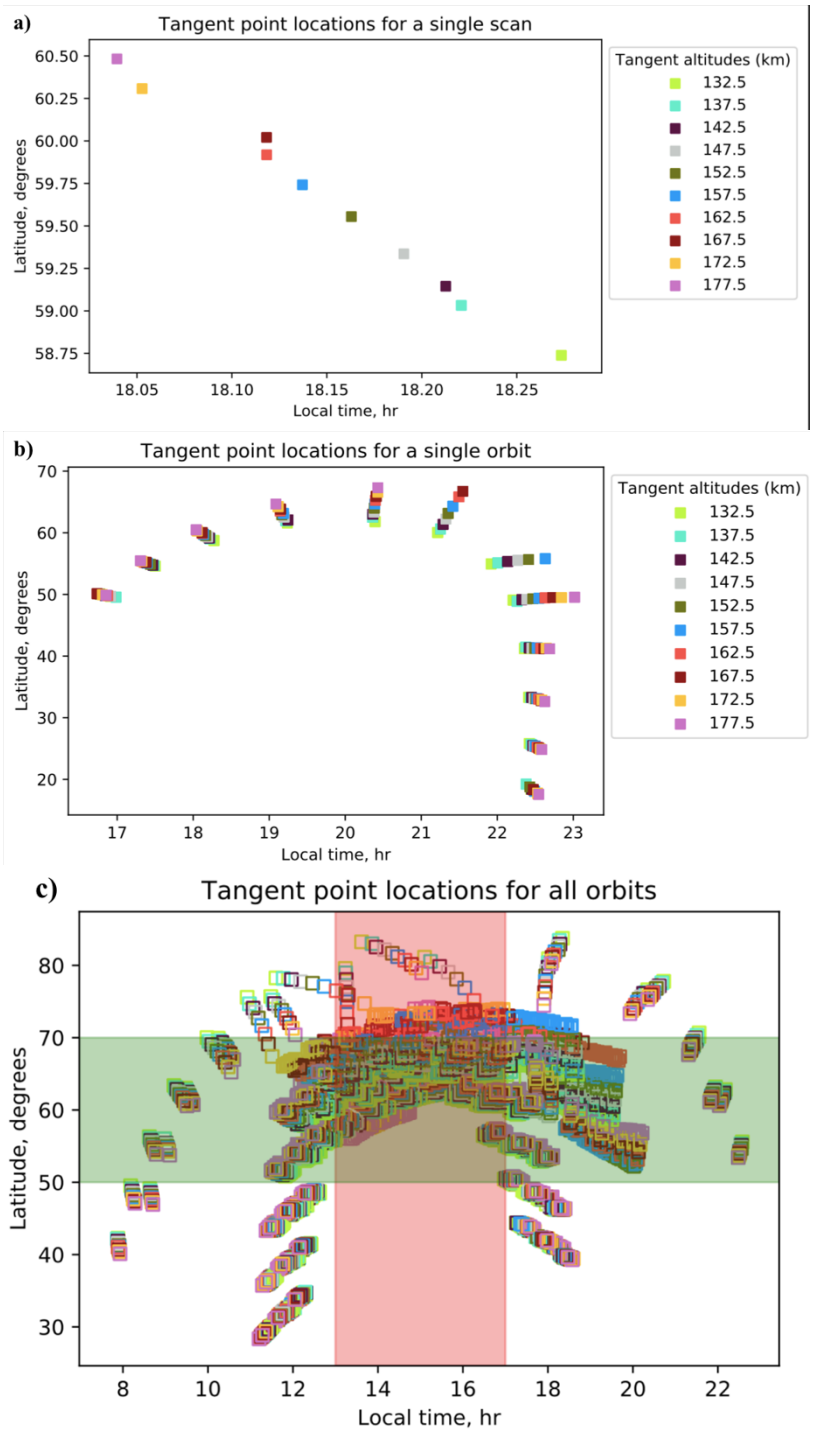

Figure 26: a) Tangent point locations between 130 – 180 km as function of latitude and local time for a single scan. b) Tangent point locations for a single orbit. c) Tangent point locations for the month of March and April 2016 with the shaded region showing the data included in the analysis for Case 1.

Figure 26a shows the tangent point locations for a single scan where all tangent altitudes lie between 130 and 180 km whereas Figure 26b shows the tangent point locations for an entire single orbit. Figure 26c shows the observations from all the orbits with each color representing the tangent point locations from a particular orbit. The clustering of data points is due to observations from multiple orbits.

Figure 27 shows that the observations from multiple orbits providing complete longitudinal coverage which is required for the analysis of tides. The data distribution plot shown in Figure 26c shows that all the measurements lie between 30° and 80° latitude. The observations chosen are narrowed down to those that lie between 50° and 70° latitude since this is region where most of the observations are made, and can be compared to the NGIMS data described in Section 3.1.5. The highlighted intersection in this plot shows the data selected and that will be used further for analysis.

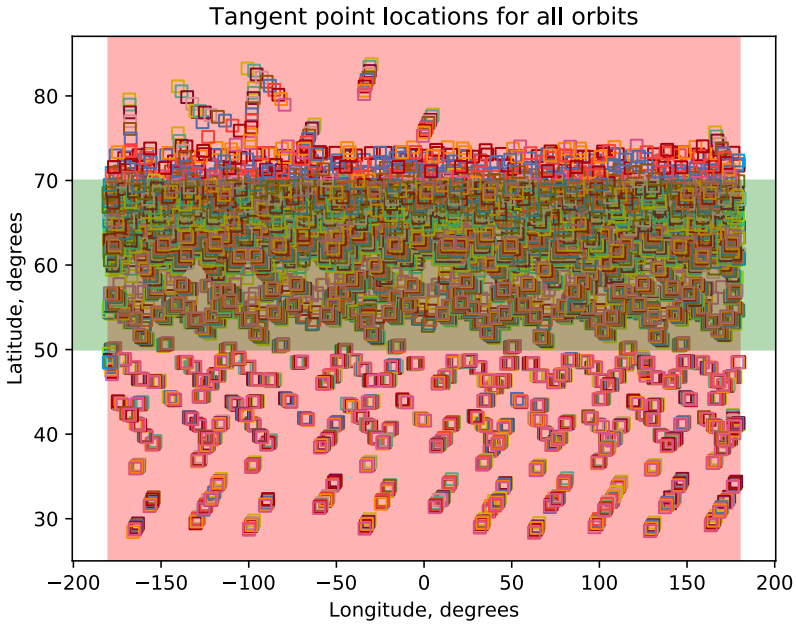

Figure 27: Tangent point locations between 130 and 180 km as a function of latitude and longitude for all orbits within the date range chosen for March and April 2016.

3.1.2 Brightness and Volume Emission Rates

The methodology adopted to identify tidal signatures is the same as that applied to the control study and described in Chapter 2. The raw brightness is first extracted based on the chosen tangent altitudes, tangent latitudes and local times. The brightnesses are then binned in 30° longitude and 10° latitude bins. The mean brightness is then averaged over 130 -180 km as a function of latitude and longitude as shown in Figure 28. Three peaks can be roughly identified at the highest latitude bin from this plot, which is closest to the NGIMS data locations. The highest latitude bin had to be cut off at 65° since there were not sufficient data points beyond the 60 - 70° bin.

The volume emission rates are plotted using the same methodology as that for the brightnesses.

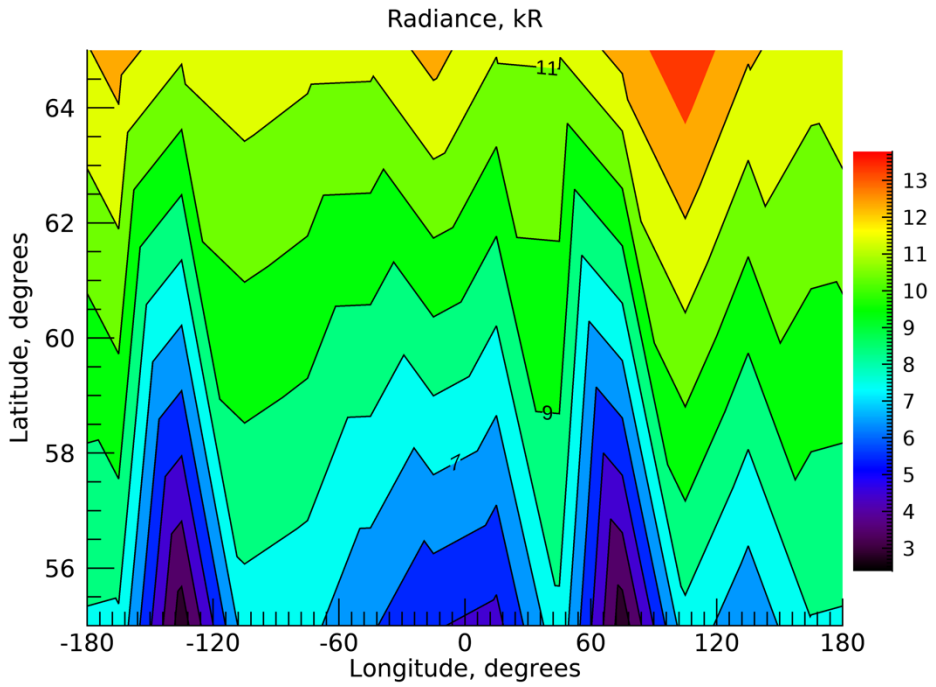

Figure 28: The mean brightness as a function of latitude and longitude averaged over the tangent altitudes between 130 and 180 km.

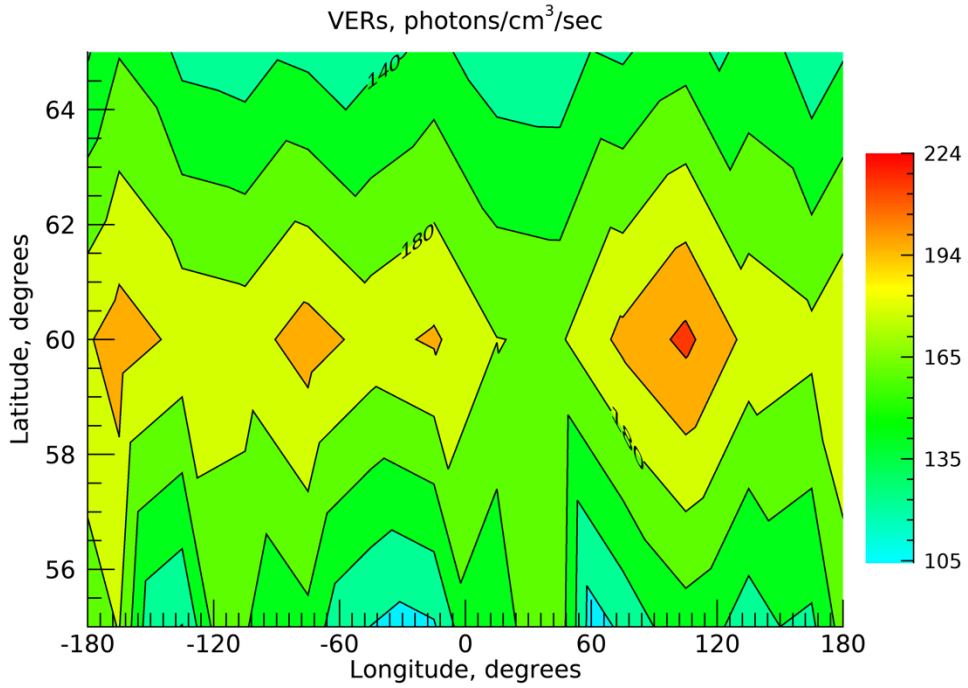

Figure 29: The mean volume emission rate as a function of latitude and longitude averaged over the tangent altitudes between 130 and 180 km.

The mean volume emission rate averaged over 130 km – 180 km as a function of latitude and longitude is shown in Figure 29. The plot shows about four peaks. The features observed in this plot could imply the variations in the volume emission rates is due to the combination of wave number 2 and wave number 3.

3.1.3 Densities and Temperatures

The derived densities and temperatures from the L2 files are plotted using the same criterion used for the volume emission rates. The mean densities are shown as a function of latitude and longitude in Figure 30.

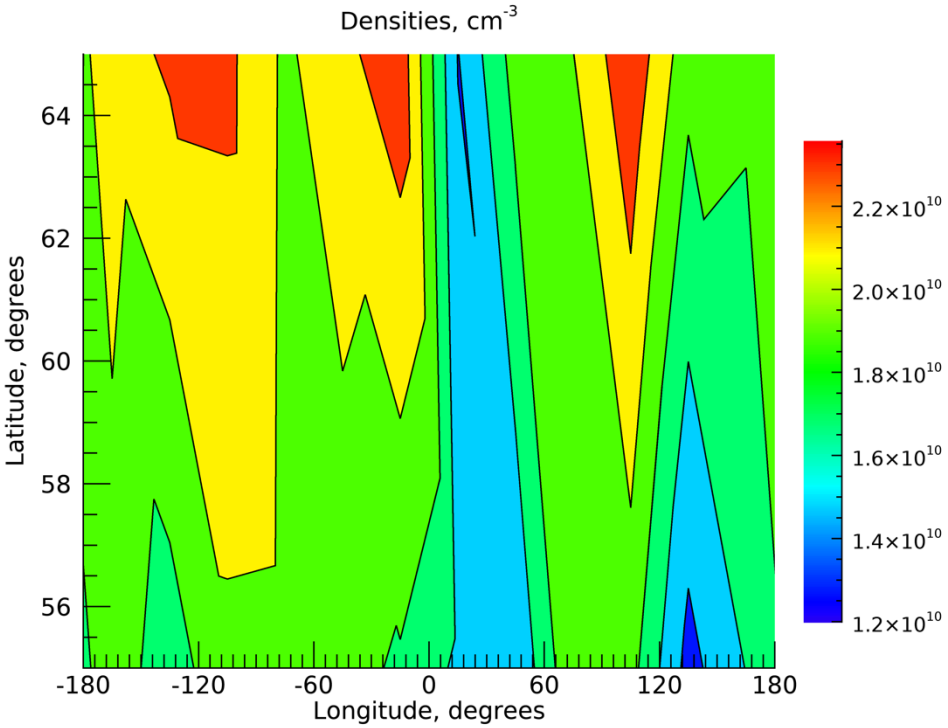

Figure 30: The mean densities as a function of latitude and longitude averaged over the tangent altitudes between 130-180 km.

Variations in densities with three distinct peaks are clearly visible from the plot around -115°, -25° and 110° respectively. The plot for the densities and volume emission rates do not match up perfectly. The peaks seen in the densities are three whereas the volume emission rates show four peaks. They are also situated higher in latitude compared to the volume emission rates. This difference could be due to the fact that the volume emission rates do not account for variability in solar conditions. As mentioned previously, the densities from the L2 files are derived taking into consideration not only the geometry of the measurements but also the insolation.

Therefore, the L2 densities will be used for the identifying the tides as well as for comparison with the NGIMS results here on. The temperatures show in Figure 31 are anti-correlated with the densities in Figure 30.

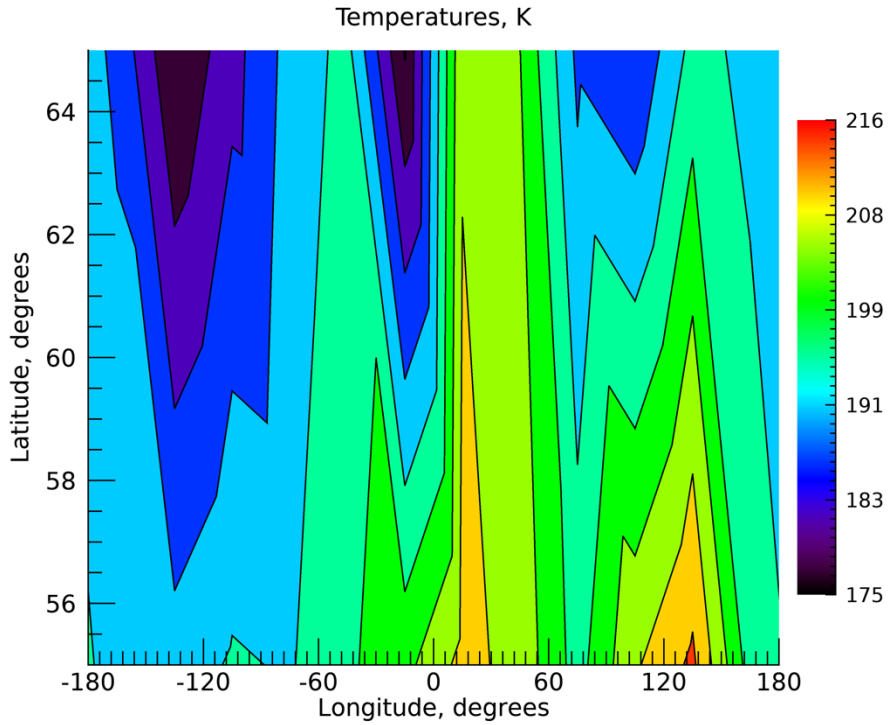

Figure 31: Mean temperatures as a function of latitude and longitude averaged over tangent altitudes between 130 and 180 km.

3.1.4 O/CO_2 *ratio*

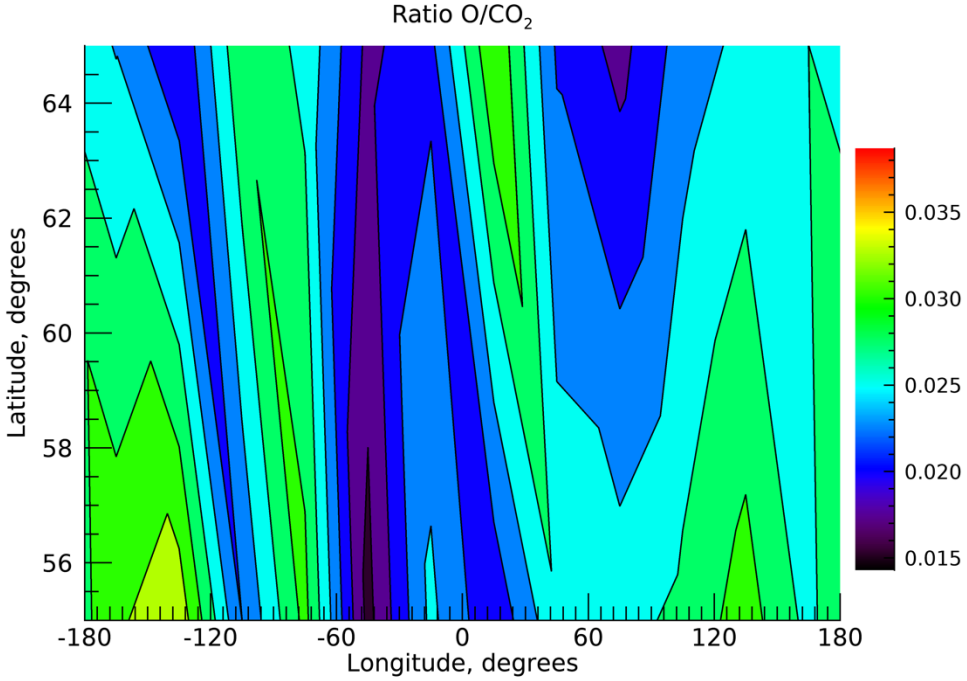

Figure 32: The O/CO_2 ratio plotted as a function of latitude and longitude.

The O and CO_2 density profiles in the L2 files are binned on a fixed altitude grid. The altitude grids for O and CO_2 are not the same and hence to find the ratio, a cubic spline interpolation was performed to retrieve densities of O and CO_2 at the same altitudes. The O/CO_2 ratio is then calculated and plotted as a function of latitude and longitude as shown in Figure 32. The plot of the ratio looks similar to the temperatures and is anti-correlated with the densities, although it is more complex.

3.1.5 Wavefits

Wavefits are performed on the density data can be seen in Figure 33 for two latitude bins centered at 55° and 65° respectively. The wave number 3 is observed to be dominant at both latitudes, with 22.3% centered at 55° and 9.2% centered a 65° respectively. The amplitudes are percentages with respect to the mean zonal densities. For the bin centered at 65° wave number 1 is observed to be nearly equally dominant with an amplitude of 8%, whereas for the one centered at 55° wave number 1 and 2 have nearly the same amplitude but much less impact in contribution.

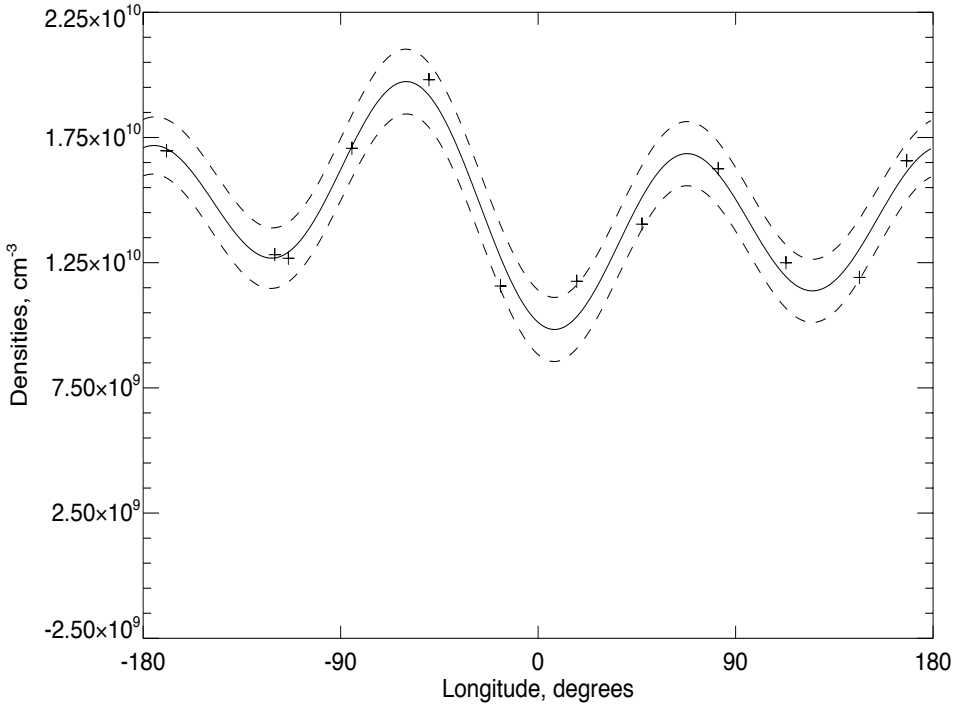

Figure 33: A wave -3 harmonic fit is done to the mean densities averaged over 130-200 km between 50° and 60N° shown by the solid line. The dashed line shows the 1σ uncertainties about the fit (solid line).

Latitude bins	Relative Amplitude Wave - 1	Relative Amplitude Wave - 2	Relative Amplitude Wave - 3	Phase Wave – 1	Phase Wave - 2	Phase Wave - 3
Centered at 55°	8.9%	7.9%	22.3%	76.65°	104.48°	3.939°
Centered at 65°	8%	5.6%	9.2%	80.38°	93.07°	24.16°

Table 4: The parameters obtained from the model fit to the densities for measurements made between 50-60°N and 60-70°N.

3.1.6 Comparison with NGIMS results

Figure 34 shows the NGIMS data distribution and coverage. The data points from March is in green and from April is in blue respectively. Figure 35 shows the CO_2 densities averaged over all latitudes as function of longitude and local time for each altitude.

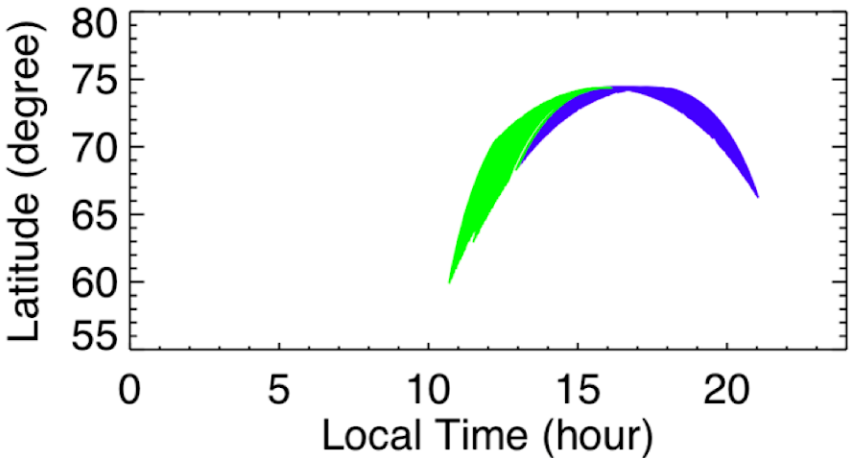

Figure 34: Data distribution of the NGIMS observations for the months of March and April 2016 shaded in green and blue respectively.

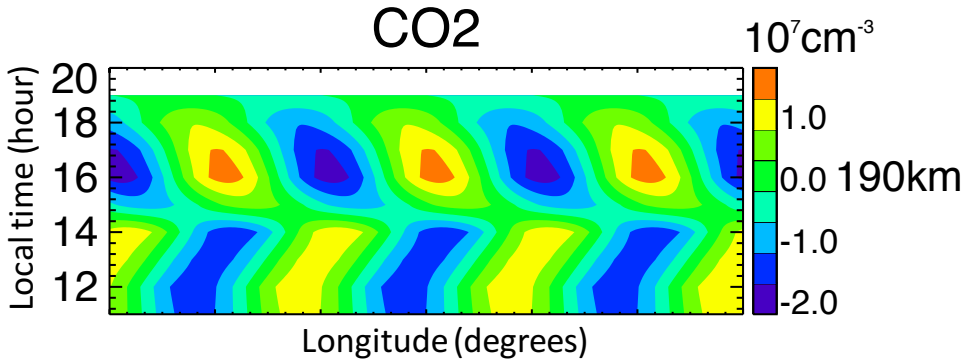

Figure 35: The mean CO_2 densities plotted as a function of longitude and local time.

The altitudes chosen here correspond to a constant CO_2 density level to enable the comparison of change in wave amplitudes between different date ranges. The constant density level picked for the NGIMS analysis was $1.3 * 10^8\ cm^{-3}$ which corresponds to an altitude of 185 km for this interval. Wave number 3 seems to dominate in this case with an eastward moving peak.

3.2 Case 2: November and December 2016

3.2.1 Data selection and availability

Case 2 includes data from orbit number 4066 to orbit number 4383. This dataset covers date ranges that fall between the 1st to 15th of November 2016 and the entire month of December 2016. Distribution of data for the entire time period is shown in Figure 36. The figures show tangent point locations of the IUVS limb observations when the tangent point is between 160 - 200 km. The tangent points are shown as a function of latitude and local time. The best overlap in latitudes for both instrument was found when the local times lie between 12 to 16 hours.

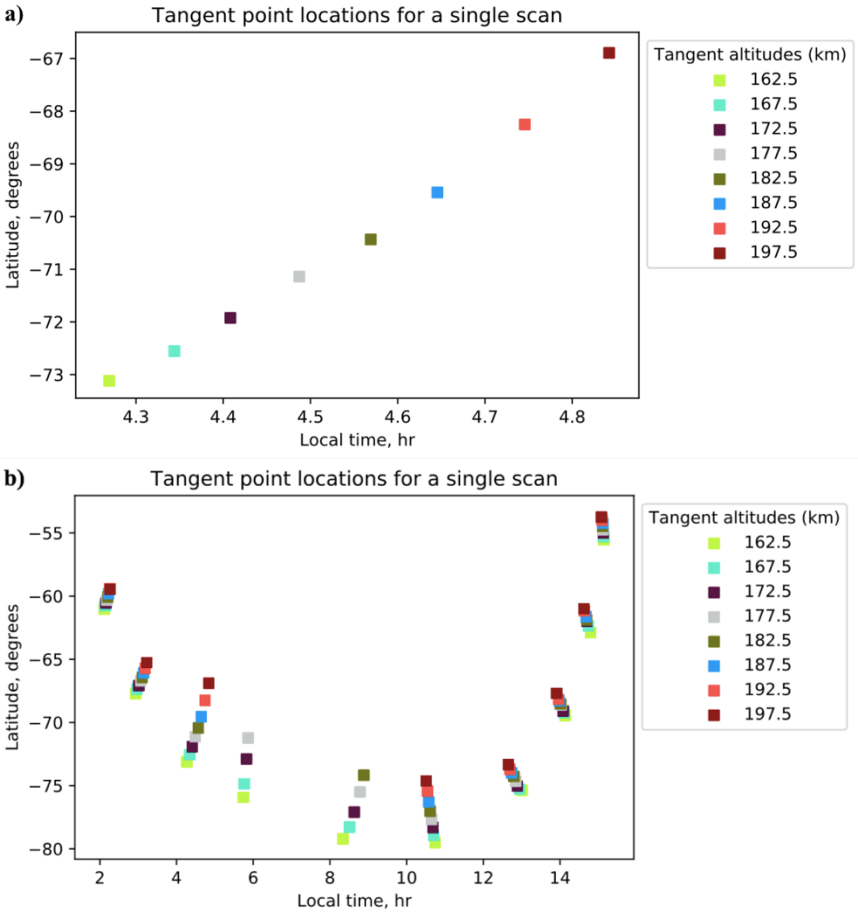

Figure 36: Tangent point locations between 160 – 200 km as function of latitude and local time for a single scan. b) Tangent point locations for a single orbit.

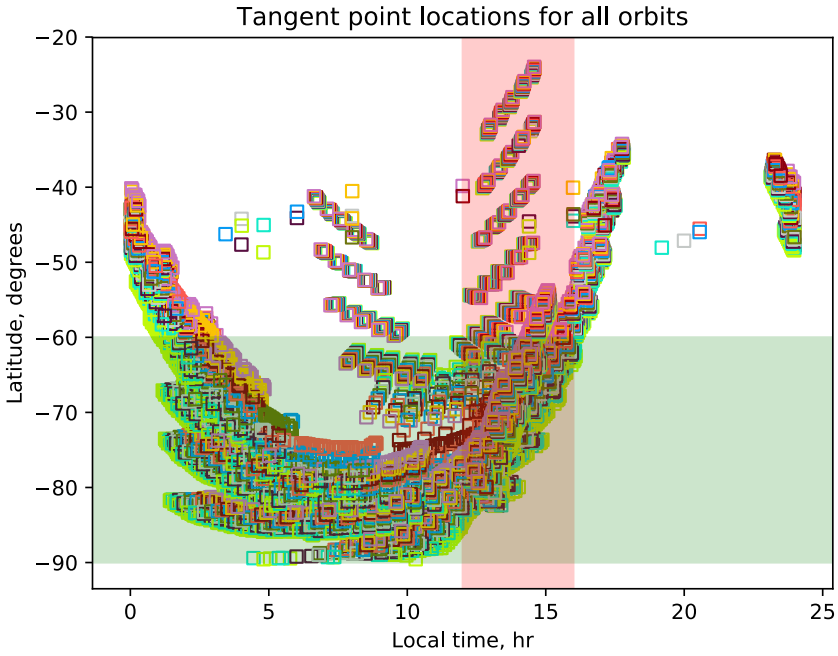

Figure 37: Tangent point locations for the months of November and December 2016 with the shaded region showing the data included in the analysis for Case 2.

3.2.2 Brightness and Volume Emission Rates

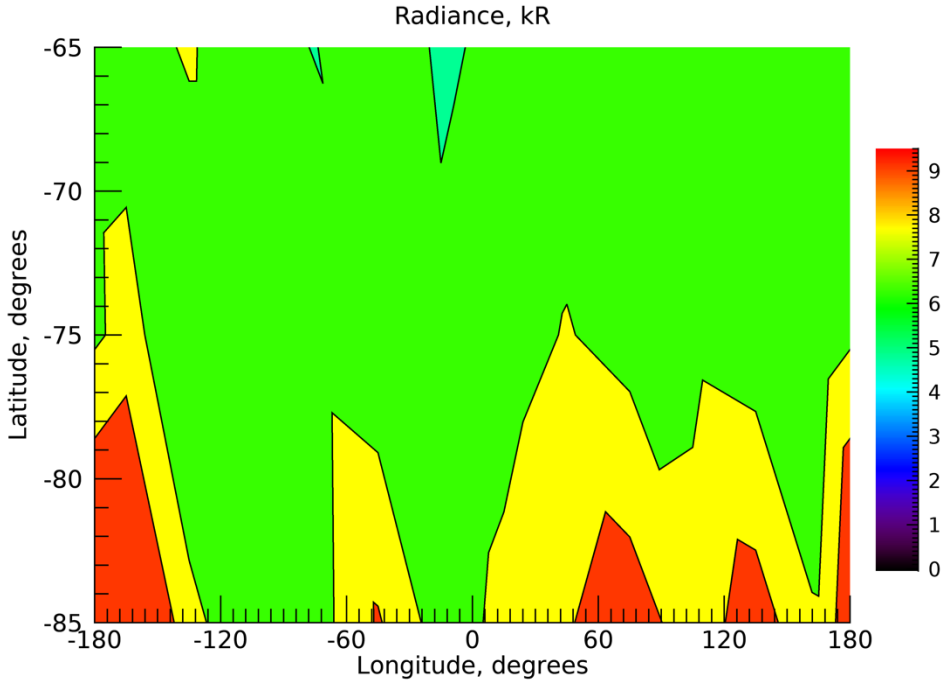

Figure 38: The mean brightness as a function of latitude and longitude averaged over the tangent altitudes between 160 and 200 km.

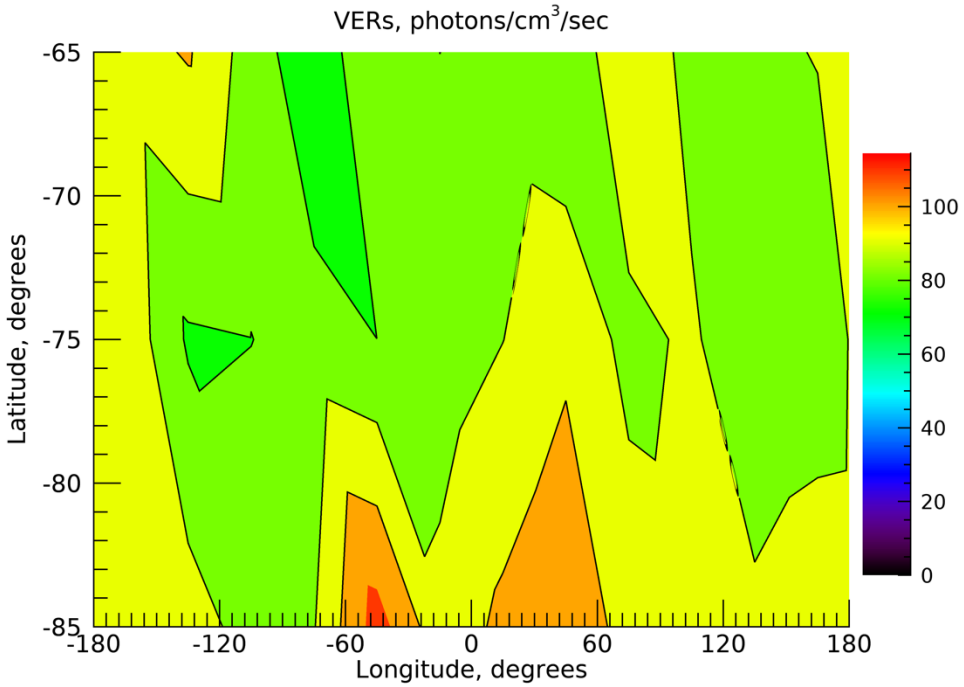

Figure 39: The mean volume emission rate as a function of latitude and longitude averaged over the tangent altitudes between 130 and 180 km.

The plot for the brightness shows some variation with about four peaks whereas in the plot for the volume emission rates the variations seem to exist at about the same locations.

3.2.3 Densities and temperatures

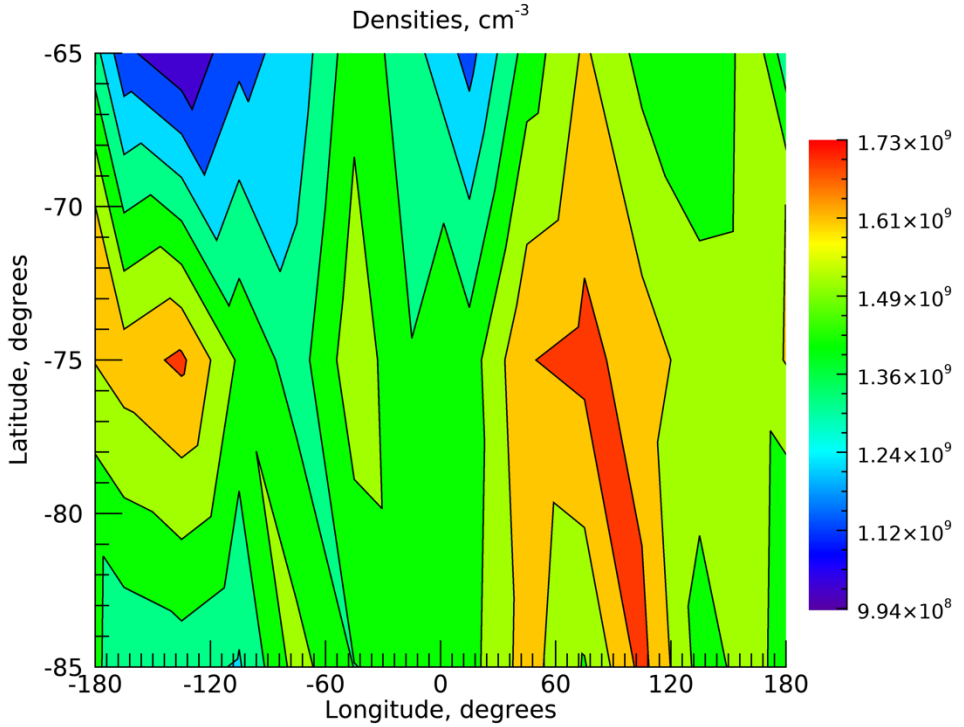

Figure 40: The mean densities as a function of latitude and longitude averaged over tangent altitudes between 160 and 200 km.

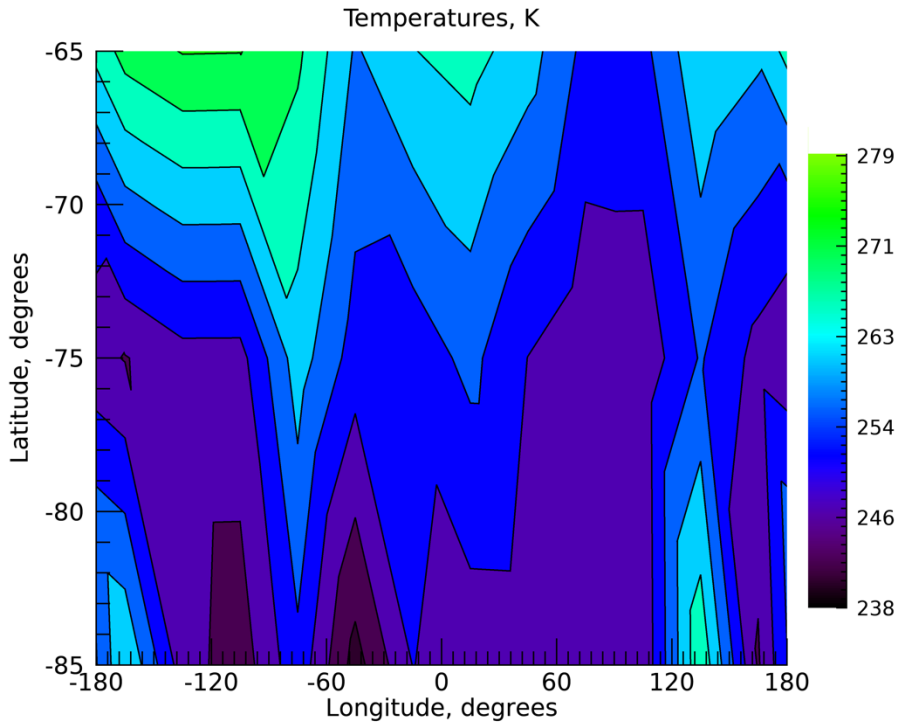

Figure 41: The mean temperatures as a function of latitude and longitude averaged over the tangent altitudes between 160 and 200 km.

The plot for the densities show variations at the latitude bin centered at -75° and roughly three peaks could be estimated at a closer look.

3.2.4 O/CO_2 *ratio*

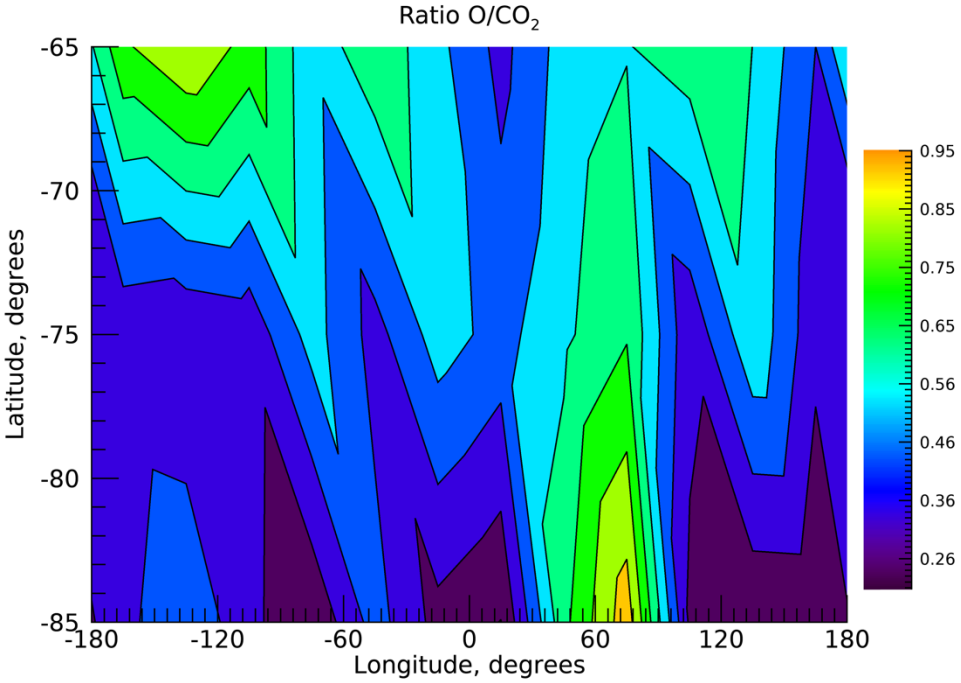

Figure 42: The mean O/CO_2 ratio as a function of latitude and longitude averaged over tangent altitudes between 160 and 200 km.

The O/CO_2 ratio seems to follow the variations seen in the temperatures and is anti-correlated with the densities which is as expected from the O/CO_2 results in Case 1.

3.2.5 Wavefits

The wavefits are performed on the density data shown in Figure 43 for the latitude bin centered at -75°. The wave number 3 is observed to dominant at this latitude with a relative amplitude of 12%. Wave-number 2 seems to be the second strongest wave with 8.5%.

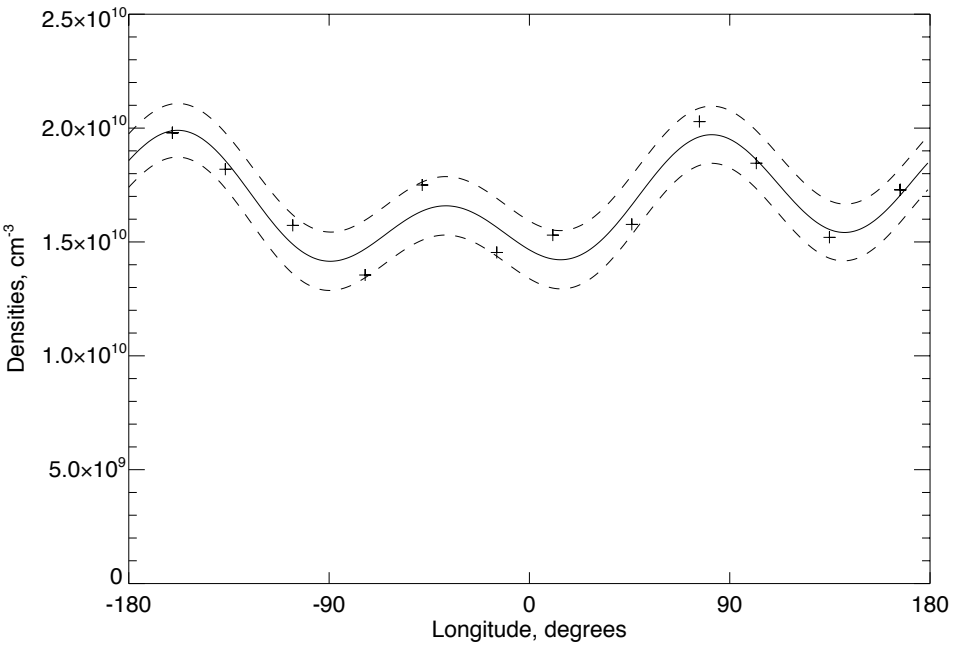

Figure 43: A wave -3 harmonic fit is done to the mean densities averaged over 160-200 km between 60° and 70°S shown by the solid line. The dashed line shows the 1σ uncertainties about the fit (solid line).

Latitude bins	Relative Amplitude Wave - 1	Relative Amplitude Wave - 2	Relative Amplitude Wave - 3	Phase Wave - 1	Phase Wave - 2	Phase Wave - 3
Centered at -75°	8.5%	4.3%	12%	323.78°	49.33°	29.06°

Table 5: The parameters obtained from the model fit to the densities for measurements made between and 70-80°S.

3.2.6 Comparison with NGIMS

The NGIMS observations allow for local time variations at the latitude bin centered at -75° and can be seen Figure 44. While the geometry perfectly lines up with the available IUVS observations, it is important to note that these are also at very high latitudes and hence solar zenith angles, where the IUVS L2 files are sometimes missing.

The NGIMS results are from a constant density level of $1.34 * 10^8$ and a corresponding altitude of 200 km for this case gives a strong wave-3 and nearly equally strong wave 2. Figure 45 shows

the fitted CO_2densities as a function of longitude and local time. It can also be seen that the observed wave-3 feature is moving eastward.

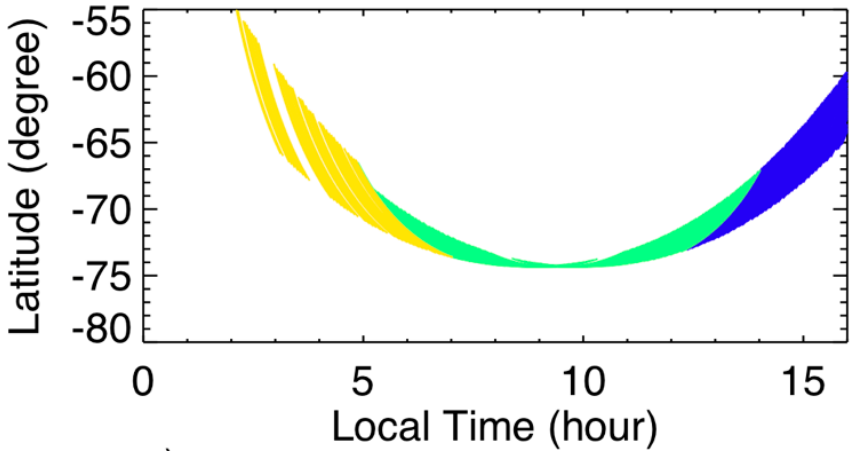

Figure 44: Data distribution of the NGIMS observations for the months of October, November and December shaded in blue, green and yellow respectively.

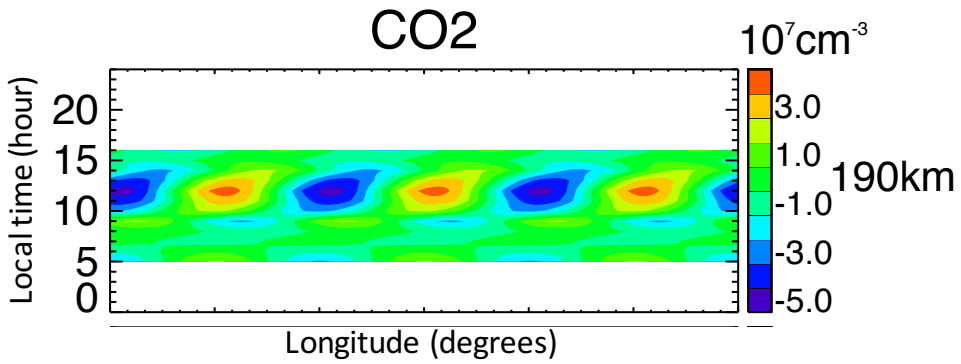

Figure 45: The mean CO2 densities plotted as a function of longitude and local time.

3.3 Case 3: May and June 2017

3.3.1 Data selection and availability

Case 3 includes data from orbit number 5119 to orbit number 5334. This dataset covers dates that fall between the 21st of May 2017 to the 30th of June 2017. Distribution of data for the entire time period is shown in Figure 46c. The figures show tangent point locations of the IUVS limb observations when the tangent point is between 150 - 200 km. The tangent points are shown as a function of latitude and local time.

The best overlap in latitudes with the NGIMS observations are when the local times lie between 9 to 12 hours. There is plenty of data from the IUVS that lie between 2 to 9 hours, but since these data points are either "night-time" data or measured at extremely high solar zenith angles, it cannot be used to determine the CO_2 densities. Therefore, the focus of Case 3 will be on observations that lie between 9 to 12 hours.

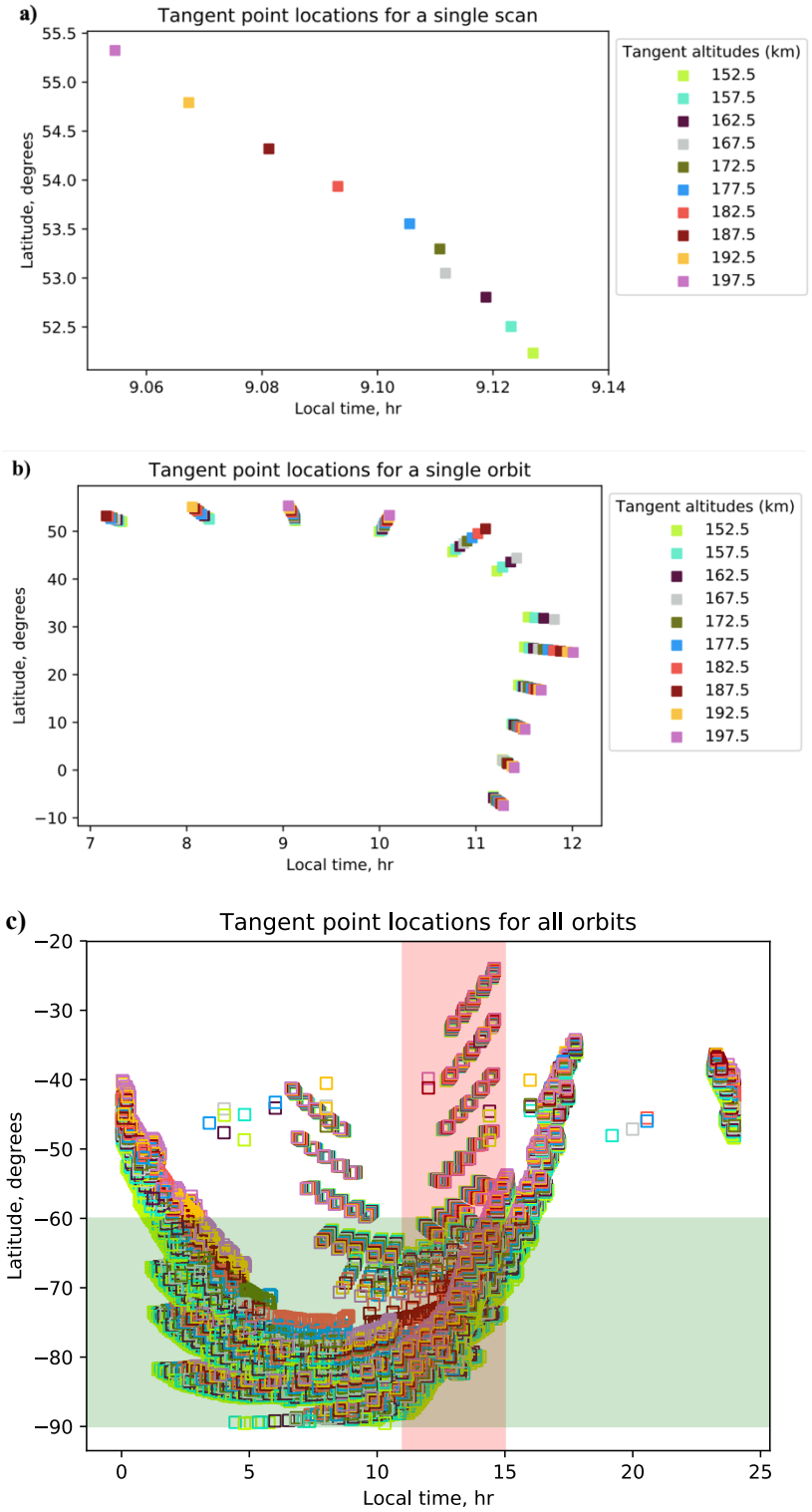

Figure 46: Tangent point locations between 150 – 200 km as function of latitude and local time for a single scan. b) Tangent point locations for a single orbit. Tangent point locations for the month of May and June 2017 with the shaded region showing the data included in the analysis for Case 3.

3.3.2 Brightness and Volume Emission Rates

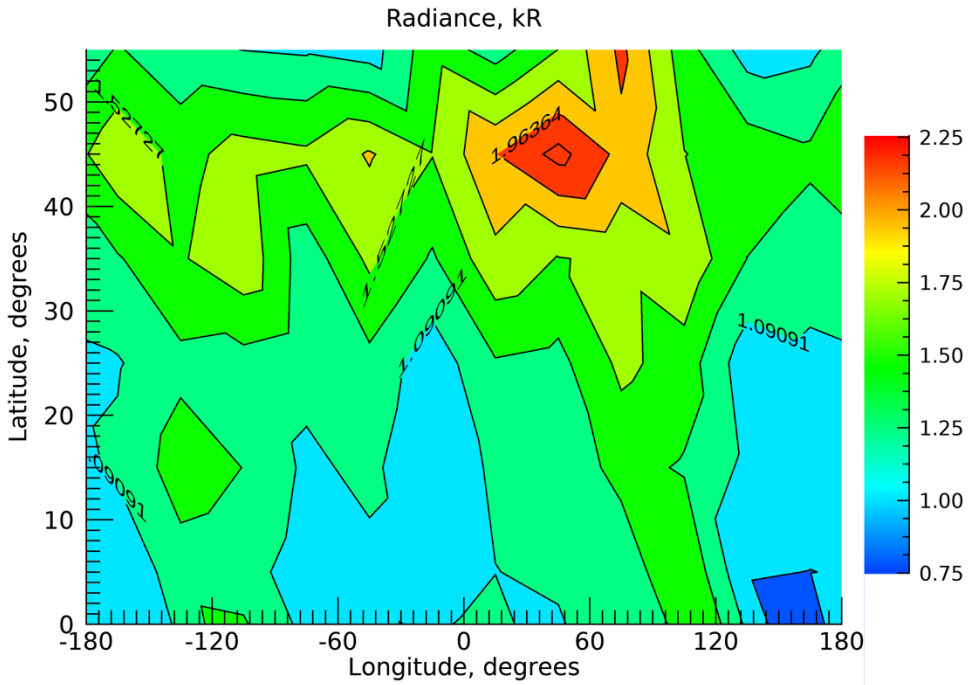

Figure 47: The mean brightness as a function of latitude and longitude averaged over the tangent altitudes between 150 and 200 km.

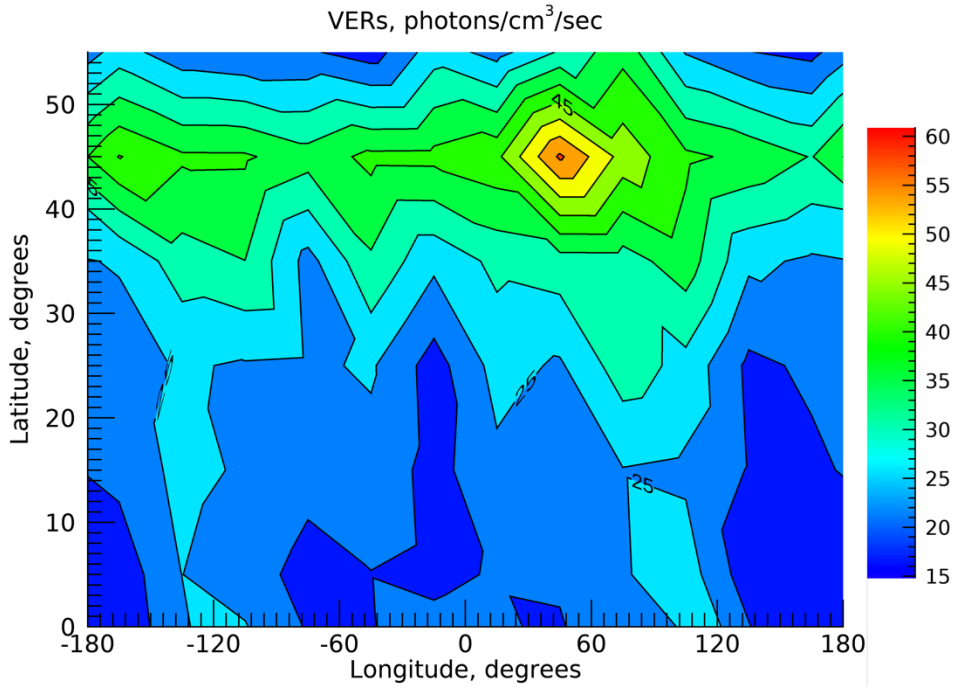

Figure 48: The mean volume emission rates as a function of latitude and longitude averaged over the tangent altitudes between 150 and 200 km.

The plot for the brightness is as shown in Figure 47. A very strong peak can be identified in this plot centered at ~60° longitude another relatively weaker one at ~-50° longitude. For Case 3, it is important to note that there is no NGIMS data below ~56° in latitude and hence no comparison will be made at the lower latitudes. The focus will be on the variations observed at latitudes close to ~45°- 55°N.

Figure 48 shows the plot of the volume emission rates with a very strong peak centered around 55° longitude. The complex structure displayed in this plot could be due to the combination of different waves.

3.3.3 Densities and Temperatures

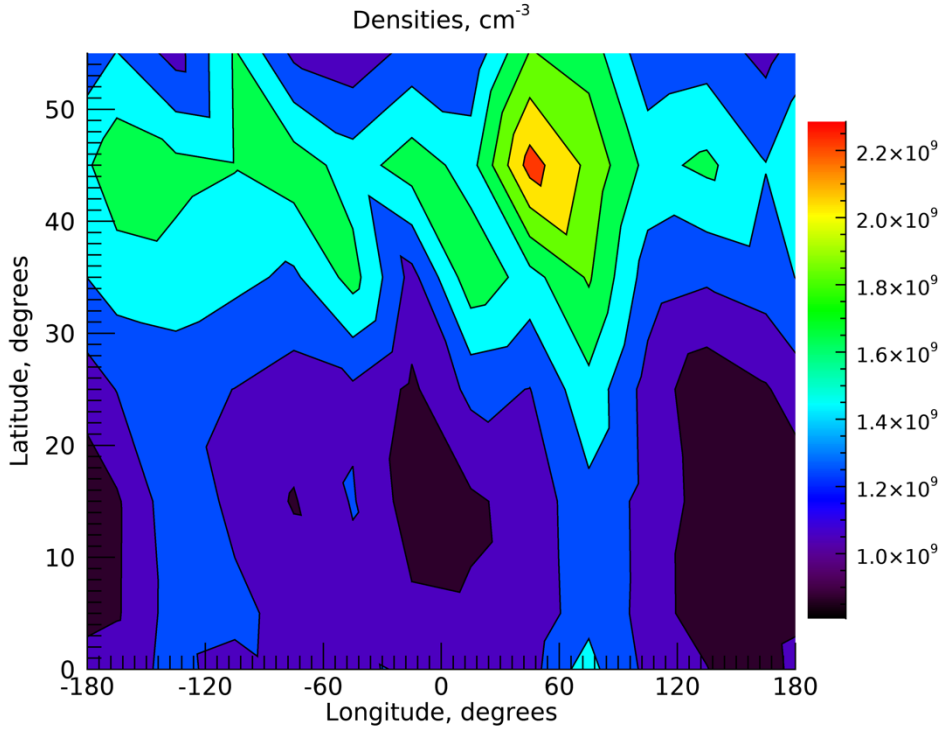

Figure 49: The mean densities as a function of latitude and longitude averaged over the tangent altitudes between 150 and 200 km.

The plot for the densities also displays a complex structure with a distinct peak at ~60° longitude. The temperatures could not be analyzed for this specific case since some of the data points were greater than two standard deviations from the mean temperature. It was necessary to set this as a criterion since some of the temperature values in the dataset were very large. On removal of the temperatures greater than two standard deviations from the mean temperature, there were insufficient data points left. One of the reasons for this could be due the fact that the observations are made for a higher solar zenith angle and early local times as in this particular case.

As for the values of the temperatures, the L2 data files are produced by utilizing an atmospheric model for initialization. The temperatures retrieved by using this method is highly sensitive to the specifics of this initialization. Details for which can be found at

https://lasp.colorado.edu/maven/sdc/public/pages/datasets/dataset_notes/iuvs_data_readme.txt. The O/CO_2 ratio also could not be plotted due to insufficient data points for the O density. Similar to the temperature values, the O density data also consisted of many bad and missing data points.

3.3.4 Wavefits

The wavefits are performed on the density data for three latitude bins centered at 25°, 35° and 45° respectively. The wave number 2 is observed to dominant in the latitude bin centered at 45° with an amplitude 10.4%. Wave-number 2 seems to be dominant at all latitudes and is strongest in the latitude bin centered at 35°. The amplitudes are percentages with respect to the mean zonal densities.

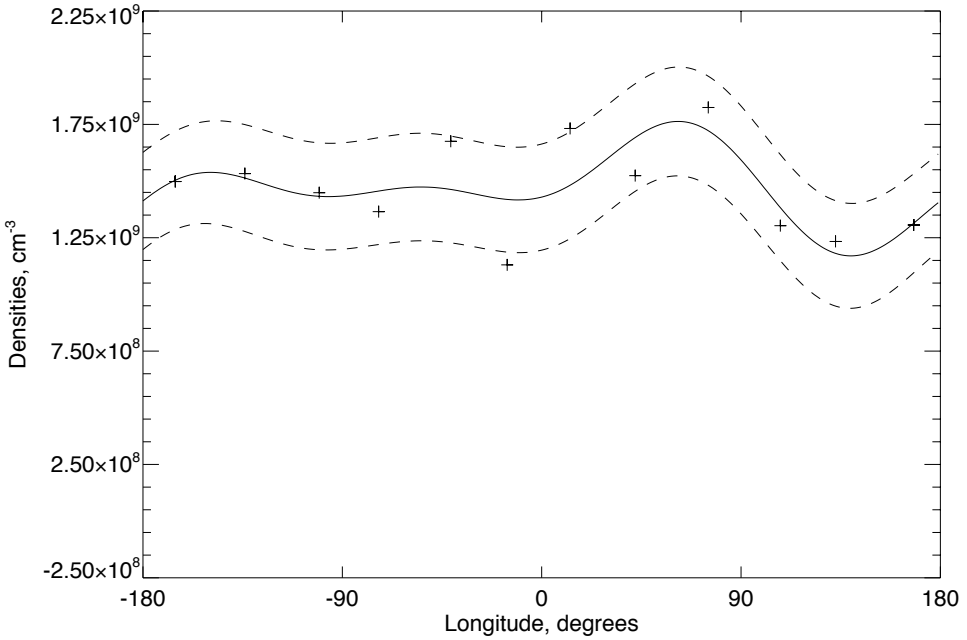

Figure 50: A wave -3 harmonic fit is done to the mean densities averaged over 150-200 km between 40° and 50N° shown by the solid line. The dashed line shows the 1σ uncertainties about the fit (solid line)

Latitude bins	Relative Amplitude Wave - 1	Relative Amplitude Wave - 2	Relative Amplitude Wave - 3	Phase Wave - 1	Phase Wave - 2	Phase Wave - 3
Centered at 25°	2%	15.1%	9.4%	160.01°	72.91°	29.32°
Centered at 35°	5%	15.2%	8.8%	205.76°	59.53°	16.06°
Centered at 45°	6.3%	10.4%	6.8%	193.74°	53.83°	11.7°

Table 6: The parameters obtained from the model fit to the densities for measurements made between 20-30°N, 30-40°N and 40-50°N.

3.3.5 Comparison with NGIMS

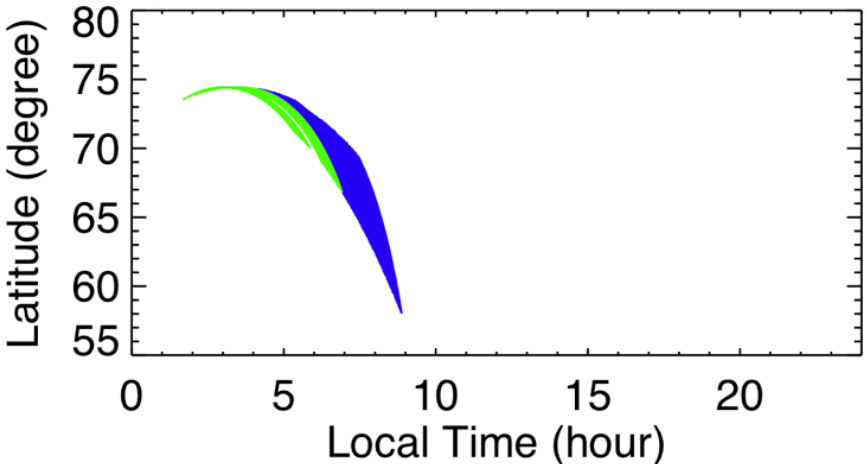

Figure 51: Data distribution of the NGIMS observations for the months of June and July shaded in blue and green respectively.

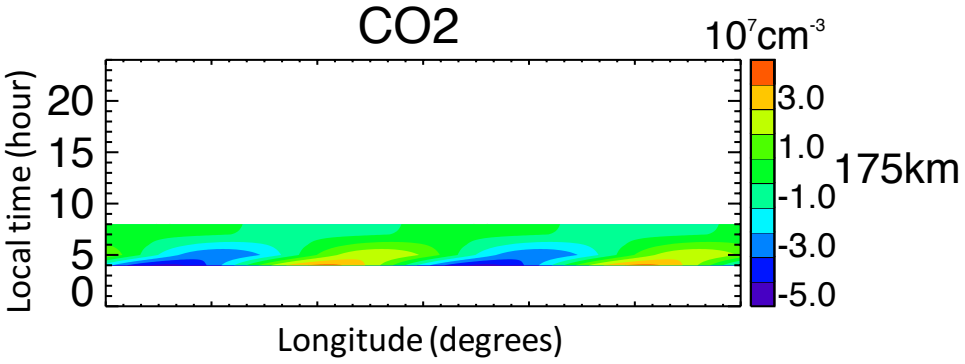

Figure 52: The mean CO2 densities plotted as a function of longitude and local time.

At the constant density level of $2.09 * 10^8$ which corresponds to 170 km for this case, the waves 2 and 3 seem to dominate with almost equivalent relative amplitudes of 24.58% and 24.53% respectively. Wave 3 seems to be dominant at 173 km and 175 km. Although the results from both instruments do not agree for this case, it is important to note that the there is very little overlap in latitudes as well as in the date range, making it impossible to draw robust conclusions from this comparison. The IUVS observations are much closer to the equator than the NGIMS.

We examined all other data sets that exist for the conditions outlined in Chapter 2, but the remaining ones consisted either of night time observations or observations that have almost no overlap in date range.

4 Conclusions

Observations from the IUVS and NGIMS instruments on MAVEN have been used to identify longitudinal variations in tidal features associated with nonmigrating tides. From the cases analyzed here, Case 1 and Case 2 show tidal features at 50 to 70° and -60 to -75°from 150 – 200 km altitude. The main conclusions have been summarized below:

- The variations observed in the densities and temperatures from the L2 files in the control study looked promising with the exception of the data gaps. It is thus evident that the amount of IUVS data required for the analysis of tides must be increased relative to the data used in the control case.

- In addition, the L2 data files are produced by accounting for the geometry as well as the solar variations and therefore is a good addition to the analysis to obtain more robust results.

- For the cases considered in this study, due to the constraints in the geometry of the IUVS and NGIMS the case studies are conducted at higher latitudes to maximize the overlap in observations.

- The IUVS results for Case 1 and Case 2 have a good agreement with the NGIMS results. Observations from both instruments not only have a good overlap in latitudes but also observe a strong wave 3.

- The densities and temperatures of Cases 1 and 2 are anti-correlated with each other thereby confirming the theoretical interpretation.

- The O/CO_2 ratios have been calculated for the first time using the IUVS observations. For cases 1 and 2 the O/CO_2 ratios are anti-correlated with the densities and follow the variations in the temperatures which is as expected.

- The phase of the wave for Case 1 do not agree with the NGIMS results. There could be multiple reasons for this such as the dates do not overlap perfectly or due the differences in altitudes or latitudes considered. The phase of the wave for Case 2 have a very good agreement using both instruments.

- For Case 3, the results are hard to interpret since the variations are much more complicated. But it is important to note that we have the least overlap in latitudes for this time period. The majority of IUVS observations are close to the equator whereas the NGIMS observations are at higher latitudes.

- The IUVS and NGIMS instruments are complimentary. Both instruments cover the same area, measure similar features but from two different perspectives. Observations from both instruments can therefore be used to independently identify tidal signatures and provide validation.

Bibliography

A. O. Nier, M. B. McElroy, 1976. Structure of the Neutral Upper Atmosphere of Mars: Results from Viking 1 and Viking 2. Science, New Series 194, 1298–1300.

Acuña, M.H., 1999. Global Distribution of Crustal Magnetization Discovered by the Mars Global Surveyor MAG/ER Experiment. Science 284, 790–793. https://doi.org/10.1126/science.284.5415.790

Andrews, D.G., Holton, J.R., Leovy, C.B., 1987. Middle atmosphere dynamics, International geophysics series. Academic Press, Orlando.

Barth, C.A., Hord, C.W., Pearce, J.B., Kelly, K.K., Anderson, G.P., Stewart, A.I., 1971. Mariner 6 and 7 Ultraviolet Spectrometer Experiment: Upper atmosphere data. Journal of Geophysical Research 76, 2213–2227. https://doi.org/10.1029/JA076i010p02213

Barth, C.A., Stewart, A.I., Hord, C.W., Lane, A.L., 1972. Mariner 9 ultraviolet spectrometer experiment: Mars airglow spectroscopy and variations in Lyman alpha. Icarus 17, 457–468. https://doi.org/10.1016/0019-1035(72)90011-5

Bougher, S.W., 2004. MGS Radio Science electron density profiles: Interannual variability and implications for the Martian neutral atmosphere. Journal of Geophysical Research 109. https://doi.org/10.1029/2003JE002154

Bougher, S.W., Cravens, T.E., Grebowsky, J., Luhmann, J., 2015. The Aeronomy of Mars: Characterization by MAVEN of the Upper Atmosphere Reservoir That Regulates Volatile Escape. Space Science Reviews 195, 423–456. https://doi.org/10.1007/s11214-014-0053-7

Bougher, S.W., Engel, S., Hinson, D.P., Forbes, J.M., 2001. Mars Global Surveyor radio science electron density profiles : Neutral atmosphere implications. Geophysical Research Letters 28, 3091–3094. https://doi.org/10.1029/2001GL012884

Bougher, S.W., Engel, S., Roble, R.G., Foster, B., 1999. Comparative terrestrial planet thermospheres: 2. Solar cycle variation of global structure and winds at equinox. Journal of Geophysical Research: Planets 104, 16591–16611. https://doi.org/10.1029/1998JE001019

England, S.L., Liu, G., Withers, P., Yiğit, E., Lo, D., Jain, S., Schneider, N.M., Deighan, J., McClintock, W.E., Mahaffy, P.R., Elrod, M., Benna, M., Jakosky, B.M., 2016. Simultaneous observations of atmospheric tides from combined in situ and remote observations at Mars from the MAVEN spacecraft: In Situ and Remote Observations of Tides. Journal of Geophysical Research: Planets 121, 594–607. https://doi.org/10.1002/2016JE004997

England, S.L., Liu, G., Yiğit, E., Mahaffy, P.R., Elrod, M., Benna, M., Nakagawa, H., Terada, N., Jakosky, B., 2017. MAVEN NGIMS observations of atmospheric gravity waves in the Martian thermosphere: Gravity Wave Observations at Mars. Journal of Geophysical Research: Space Physics. https://doi.org/10.1002/2016JA023475

Forbes, J.M., Bridger, A.F.C., Bougher, S.W., Hagan, M.E., Hollingsworth, J.L., Keating, G.M., Murphy, J., 2002. Nonmigrating tides in the thermosphere of Mars: NONMIGRATING

TIDES IN THE THERMOSPHERE OF MARS. Journal of Geophysical Research: Planets 107, 23-1-23–12. https://doi.org/10.1029/2001JE001582

Forbes, J.M., Hagan, M.E., 2000. Diurnal Kelvin wave in the atmosphere of Mars: Towards an understanding of 'stationary' density structures observed by the MGS accelerometer. Geophysical Research Letters 27, 3563–3566. https://doi.org/10.1029/2000GL011850

Haberle, R.M., Clancy, R.T., Forget, F., Smith, M.D., Zurek, R.W. (Eds.), 2017. The atmosphere and climate of Mars, Cambridge planetary science. Cambridge University Press, Cambridge.

Jain, S.K., Stewart, A.I.F., Schneider, N.M., Deighan, J., Stiepen, A., Evans, J.S., Stevens, M.H., Chaffin, M.S., Crismani, M., McClintock, W.E., Clarke, J.T., Holsclaw, G.M., Lo, D.Y., Lefèvre, F., Montmessin, F., Thiemann, E.M.B., Eparvier, F., Jakosky, B.M., 2015. The structure and variability of Mars upper atmosphere as seen in MAVEN/IUVS dayglow observations: IUVS DAYGLOW OBSERVATIONS. Geophysical Research Letters 42, 9023–9030. https://doi.org/10.1002/2015GL065419

Jakosky, B.M., Lin, R.P., Grebowsky, J.M., Luhmann, J.G., Mitchell, D.F., Beutelschies, G., Priser, T., Acuna, M., Andersson, L., Baird, D., Baker, D., Bartlett, R., Benna, M., Bougher, S., Brain, D., Carson, D., Cauffman, S., Chamberlin, P., Chaufray, J.-Y., Cheatom, O., Clarke, J., Connerney, J., Cravens, T., Curtis, D., Delory, G., Demcak, S., DeWolfe, A., Eparvier, F., Ergun, R., Eriksson, A., Espley, J., Fang, X., Folta, D., Fox, J., Gomez-Rosa, C., Habenicht, S., Halekas, J., Holsclaw, G., Houghton, M., Howard, R., Jarosz, M., Jedrich, N., Johnson, M., Kasprzak, W., Kelley, M., King, T., Lankton, M., Larson, D., Leblanc, F., Lefevre, F., Lillis, R., Mahaffy, P., Mazelle, C., McClintock, W., McFadden, J., Mitchell, D.L., Montmessin, F., Morrissey, J., Peterson, W., Possel, W., Sauvaud, J.-A., Schneider, N., Sidney, W., Sparacino, S., Stewart, A.I.F., Tolson, R., Toublanc, D., Waters, C., Woods, T., Yelle, R., Zurek, R., 2015. The Mars Atmosphere and Volatile Evolution (MAVEN) Mission. Space Science Reviews 195, 3–48. https://doi.org/10.1007/s11214-015-0139-x

Keating et al., 2003. WINTER POLAR CONDITIONS IN THE MARS UPPER ATMOSPHERE AT BOTH THE NORTH AND SOUTH POLES 5.

Keating et al., 1998. The Structure of the Upper Atmosphere of Mars: In Situ Accelerometer Measurements from Mars Global Surveyor Author(s): G. M. Keating, S. W. Bougher, R. W. Zurek, R. H. Tolson, G. J. Cancro, S. N. Noll, J. S. Parker, T. J. Schellenberg, R. W. Shane, B. L. Wilkerson, J. R. Murphy, J. L. Hollingsworth, R. M. Haberle, M. Joshi, J. C. Pearl, B. J. Conrath, M. D. Smith, R. T. Clancy, R. C. Blanchard, R. G. Wilmoth, D. F. Rault, T. Z. Martin, D. T. Lyons, P. B. Esposito, M. D. Johnston, C. W. Whetzel, C. G. Justus and J. M. Babicke. Science, New Series 279, 1672–1676.

Liu, G., England, S., Lillis, R.J., Mahaffy, P.R., Elrod, M., Benna, M., Jakosky, B., 2017. Longitudinal structures in Mars' upper atmosphere as observed by MAVEN/NGIMS: UPPER ATMOSPHERE LONGITUDINAL STRUCTURES. Journal of Geophysical Research: Space Physics 122, 1258–1268. https://doi.org/10.1002/2016JA023455

Lo, D.Y., Yelle, R.V., Schneider, N.M., Jain, S.K., Stewart, A.I.F., England, S.L., Deighan, J.I., Stiepen, A., Evans, J.S., Stevens, M.H., Chaffin, M.S., Crismani, M.M.J., McClintock, W.E., Clarke, J.T., Holsclaw, G.M., Lefèvre, F., Jakosky, B.M., 2015. Nonmigrating

tides in the Martian atmosphere as observed by MAVEN IUVS: MARS ATMOSPHERIC TIDES FROM MAVEN/IUVS. Geophysical Research Letters 42, 9057–9063. https://doi.org/10.1002/2015GL066268

Mahaffy, P.R., Benna, M., King, T., Harpold, D.N., Arvey, R., Barciniak, M., Bendt, M., Carrigan, D., Errigo, T., Holmes, V., Johnson, C.S., Kellogg, J., Kimvilakani, P., Lefavor, M., Hengemihle, J., Jaeger, F., Lyness, E., Maurer, J., Melak, A., Noreiga, F., Noriega, M., Patel, K., Prats, B., Raaen, E., Tan, F., Weidner, E., Gundersen, C., Battel, S., Block, B.P., Arnett, K., Miller, R., Cooper, C., Edmonson, C., Nolan, J.T., 2015. The Neutral Gas and Ion Mass Spectrometer on the Mars Atmosphere and Volatile Evolution Mission. Space Science Reviews 195, 49–73. https://doi.org/10.1007/s11214-014-0091-1

Mars24 Sunclock — Time on Mars, n.d.

McClintock, W.E., Schneider, N.M., Holsclaw, G.M., Clarke, J.T., Hoskins, A.C., Stewart, I., Montmessin, F., Yelle, R.V., Deighan, J., 2015. The Imaging Ultraviolet Spectrograph (IUVS) for the MAVEN Mission. Space Science Reviews 195, 75–124. https://doi.org/10.1007/s11214-014-0098-7

Medvedev, A.S., Nakagawa, H., Mockel, C., Yiğit, E., Kuroda, T., Hartogh, P., Terada, K., Terada, N., Seki, K., Schneider, N.M., Jain, S.K., Evans, J.S., Deighan, J.I., McClintock, W.E., Lo, D., Jakosky, B.M., 2016. Comparison of the Martian thermospheric density and temperature from IUVS/MAVEN data and general circulation modeling: IUVS-MGCM COMPARISON. Geophysical Research Letters 43, 3095–3104. https://doi.org/10.1002/2016GL068388

Stiepen, A., Gérard, J.-C., Bougher, S., Montmessin, F., Hubert, B., Bertaux, J.-L., 2015. Mars thermospheric scale height: CO Cameron and CO2+ dayglow observations from Mars Express. Icarus 245, 295–305. https://doi.org/10.1016/j.icarus.2014.09.051

Withers, P., Bougher, S.., Keating, G.., 2003. The effects of topographically-controlled thermal tides in the martian upper atmosphere as seen by the MGS accelerometer. Icarus 164, 14–32. https://doi.org/10.1016/S0019-1035(03)00135-0

Withers, P., Pratt, R., Bertaux, J.-L., Montmessin, F., 2011. Observations of thermal tides in the middle atmosphere of Mars by the SPICAM instrument. Journal of Geophysical Research 116. https://doi.org/10.1029/2011JE003847

Zurek, R.W., 1976. Diurnal Tide in the Martian Atmosphere. Journal of the Atmospheric Sciences 33, 321–337. https://doi.org/10.1175/1520-0469(1976)033<0321:DTITMA>2.0.CO;2